Please provide feedback

Please support the ScholarWorks@UMBC repository by emailing scholarworks-group@umbc.edu and telling us what having access to this work means to you and why it's important to you. Thank you.

Radio–gamma-ray connection and spectral evolution in 4C +49.22 (S4 1150+49): the *Fermi*, *Swift* and *Planck* view

S. Cutini,[1,2]★ S. Ciprini,[1,2] M. Orienti,[3,4] A. Tramacere,[5] F. D'Ammando,[3,6,7]
F. Verrecchia,[1,2] G. Polenta,[1,2] L. Carrasco,[8] V. D'Elia,[1,2] P. Giommi,[1]
J. González-Nuevo,[9,10] P. Grandi,[11] D. Harrison,[12,13] E. Hays,[14] S. Larsson,[15,16,17]
A. Lähteenmäki,[18,19] J. León-Tavares,[20,21] M. López-Caniego,[9] P. Natoli,[1,22] R. Ojha,[14]
B. Partridge,[23] A. Porras,[8] L. Reyes,[24] E. Recillas[8] and E. Torresi[11]

Affiliations are listed at the end of the paper

ABSTRACT

The Large Area Telescope on board the *Fermi Gamma-ray Space Telescope* detected a strong γ-ray flare on 2011 May 15 from a source identified as 4C +49.22, a flat spectrum radio quasar (FSRQ) also known as S4 1150+49. This blazar, characterized by a prominent radio–optical–X-ray jet, was in a low γ-ray activity state during the first years of *Fermi* observations. Simultaneous observations during the quiescent, outburst and post-flare γ-ray states were obtained by *Swift*, *Planck* and optical–IR–radio telescopes (Instituto Nacional de Astrofísica, Óptica y Electrónica, Catalina Sky Survey, Very Long Baseline Array [VLBA], Metsähovi). The flare is observed from microwave to X-ray bands with correlated variability and the *Fermi*, *Swift* and *Planck* data for this FSRQ show some features more typical of BL Lac objects, like the synchrotron peak in the optical band that outshines the thermal blue-bump emission, and the X-ray spectral softening. Multi-epoch VLBA observations show the ejection of a new component close in time with the GeV γ-ray flare. The radio-to-γ-ray spectral energy distribution is modelled and fitted successfully for the outburst and the post-flare epochs using either a single flaring blob with two emission processes (synchrotron self-Compton (SSC), and external-radiation Compton), and a two-zone model with SSC-only mechanism.

Key words: galaxies: active – galaxies: jets – quasars: general – quasars: individual: 4C +49.22 – gamma-rays: galaxies – X-rays: galaxies.

1 INTRODUCTION

Data and results from simultaneous and coordinated γ-ray and multiwavelength (MW) observations of the flat spectrum radio quasar (FSRQ) 4C +49.22 (also known as S4 1150+49, OM 484, SBS 1150+497 and GB1 1150+497), are presented.

4C +49.22 is a core-dominated, radio-loud FSRQ located at $z = 0.334$ (Burbidge 1968; Lynds & Wills 1968; Stepanian et al. 2001). The Sloan Digital Sky Survey (SDSS; Adelman-McCarthy et al. 2008) DR7 and DR8 give values of $z = 0.3339$ and of $z = 0.33364$, respectively. This blazar shows a kiloparsec-extent and one-sided, knotty and wiggling radio jet, with high surface brightness, sharp bends and resolved substructures (see e.g. Owen & Puschell 1984; Akujor & Garrington 1991; Sambruna et al. 2004, 2006a,b). The jet, known to show constant low optical polarization (Moore & Stockman 1981), has a twisted morphology with a corkscrew structure reminiscent of 3C 273 and, remarkably, is also well detected at X-ray and optical bands. The 10 arcsec X-ray jet of 4C +49.22 is one of the brightest known among blazars, and is an example of X-ray emission produced by inverse Compton (IC) scattering of the cosmic microwave background (CMB) photons (Tavecchio et al. 2005; Hardcastle 2006; Sambruna et al. 2006a).

The *Chandra X-ray Observatory* detected an Fe K-shell emission line in 4C +49.22 consistent with fluorescent $K\alpha$ emission from cold iron (Gambill et al. 2003; Sambruna et al. 2006a,b). The estimated mass of the supermassive black hole (SMBH) is 3.3×10^8 M$_\odot$ according to the full width at half-maximum (FWHM) of the broad Hβ line (4810 km s^{-1}; Shields et al. 2003) and is 1.6×10^9 M$_\odot$ according to the estimation from the host galaxy luminosity (Decarli et al. 2008). From the SDSS R5 spectrum the continuum luminosity of the broad line region (BLR) at 5100 Å is evaluated to be $F_\lambda = 10^{44.6}$ erg s^{-1} with a BLR size of $R_{\rm BLR} = 1.26 \times 10^{17}$ cm (Decarli et al. 2008).

4C +49.22 showed a large γ-ray outburst detected with the Large Area Telescope (LAT) onboard the *Fermi Gamma-ray Space*

★ E-mail: sara.cutini@asdc.asi.it

Telescope (*Fermi*-LAT), at energies above 100 MeV on 2011 May 15 (Reyes, D'Ammando & Hoversten 2011). Before this flaring event the source was in a long-standing quiescent state with no detection reported in the first *Fermi*-LAT source catalogue (Abdo et al. 2010a) or in previous source catalogues released by other MeV–GeV γ-ray missions like EGRET (Hartman et al. 1999) and AGILE (Pittori et al. 2009). It was included in the second *Fermi*-LAT source catalogue (Nolan et al. 2012, 2FGL hereafter; 2FGL J1153.2+4935) with a 2-yr averaged γ-ray flux ($E > 100$ MeV) of $(2.6 \pm 0.4) \times 10^{-8}$ photons cm^{-2} s^{-1}. During the flare the source reached a flux almost two orders of magnitude higher than the 2FGL average flux. The source was significantly detected on a daily time-scale in 2011 April (Hays & Donato 2011). The γ-ray spectrum did not show significant changes during the outburst compared to the pre- and post-flare days. In the post-flare phase, *Swift*-XRT (X-ray telescope) reported an X-ray flux six times higher than previous archival XRT observations (Reyes et al. 2011). This FSRQ was also observed with the *Planck* satellite. According to the *Planck*-On-the-Fly Forecaster (Massardi & Burigana 2010), 4C +49.22 was observed by *Planck* from 2011 May 11 to 26. We exploited *Planck*, *Swift* and *Fermi* simultaneous data, for the first time, to study this blazar. We collected spectral energy distribution (SED) archival data from several surveys and telescopes, from radio to γ rays: Dixon Master List of Radio Sources (Dixon 1970); the FIRST Survey Catalog of 1.4-GHz Radio Sources (White et al. 1997); Kuehr Extragalactic Radio Sources at 5 GHz (Kuehr et al. 1981); the NRAO VLA Sky Survey (Condon et al. 1998); the VLA Low-Frequency Sky Survey at 74 MHz (Cohen et al. 2007); the Green Bank 6-cm Catalog of Radio Sources (Gregory et al. 1996); the 20-cm Northern Sky Catalog; the *Planck* Early Release Compact Source Catalogue (ERCSC; Planck Collaboration VII 2011c); Five-Year *Wilkinson Microwave Anisotropy Probe* (*WMAP*; Wright et al. 2009); the SDSS; the *ROSAT* All-Sky Survey Bright Source Catalogue (Voges et al. 1999), the *ROSAT* Catalogue of PSPC WGA Sources (White, Giommi & Angelini 1994); and the 2FGL catalogue.

The paper is organized as follows. In Section 2, the *Fermi*-LAT data analysis is presented, while in Section 3 the millimetre *Planck* data from the sky coverages with *Planck* are described, with particular attention to the fourth sky scan that is coincident in time with the 2011 May γ-ray outburst. In Section 4 optical, UV and X-ray data from nine *Swift* pointings under the Target of Opportunity programme (ToO) performed between 2011 April 26 and May 25 are presented. Section 5 reports on ground-based radio-to-optical observations obtained by the VLBA (Monitoring Of Jets in Active galactic nuclei with VLBA Experiments [MOJAVE] monitoring programme) and Metsähovi radio observatories, and by near-IR and optical photometric observations of the Instituto Nacional de Astrofísica, Óptica y Electrónica (INAOE) observatory and the Catalina Sky Survey (CSS). Section 6 characterizes the γ-ray variability and cross-correlations in 4C +49.22 through 3 yr of *Fermi*-LAT survey data, with particular focus on the outburst of 2011 May. Multi-epoch SEDs are built for the source and modelled with a one-zone with two components synchrotron self-Compton (SSC) and external-radiation Compton (ERC) description and a two-zone SSC description in Section 7. This allows us to infer both the production sites of the high-energy emission and emission scenarios. A summary and conclusions are reported in Section 8. We adopted a standard spatially flat six-parameter Λ cold dark matter cosmology based on *Planck* results (Ade et al. 2013), namely with $\Omega_m = 0.315$ and $H_0 = 67.3$ km s^{-1} Mpc^{-1}. The corresponding luminosity distance at $z = 0.334$ is $d_L = 1822.3$ Mpc.

2 γ-RAY OBSERVATIONS AND ANALYSIS OF FERMI-LAT DATA

The LAT instrument is a pair conversion telescope comprising a modular array of 16 towers – each with a tracker module of silicon micro-strip detectors and a hodoscopic calorimeter of CsI(Tl) crystals – surrounded by an Anti-Coincidence Detector made of tiles of plastic scintillator. The LAT is capable of measuring the directions and energies of γ-ray photons with energies from 20 MeV to >300 GeV (for details, see Abdo et al. 2009a; Atwood et al. 2009; Ackermann et al. 2012).

The data presented in this paper were collected in the first 3 yr of *Fermi* science observations, from 2008 August 4 to 2011 August 4 (MJD 54682–55778) with $E > 100$ MeV. Photon events were selected using the Pass 7 event classification and reconstruction and the corresponding instrument response functions P7SOURCE_V6. This selection provides a clean set of events (in terms of direction, energy reconstruction and background rejection) a large effective area and well understood response functions for point source analysis. To minimize contamination from photons produced by cosmic rays interacting with the Earth's atmosphere, γ-ray events that have reconstructed directions with angles >100° with respect to the local zenith have been excluded and the time intervals when the rocking angle of the LAT was greater than 52° were rejected.

The reduction and analysis of LAT data was performed using the SCIENCETOOLS v09r23p01,[1] specifically using an unbinned maximum-likelihood estimator of the spectral model parameters (GTLIKE tool). For 4C +49.22, which is located at high Galactic latitude, events are extracted within a 10° radius of the region of interest (ROI) centred at the position of the radio source counterpart. This angular radius, comparable to the 68 per cent containment angle of the point spread function (PSF)[2] at the lowest energies, provides sufficient events to accurately constrain the diffuse emission components. Following the 2FGL catalogue, the spectral model used for 4C +49.22 is the power-law flux density distribution of the form $F(E) = N_0(E/E_0)^{-\Gamma}$. The source region model includes all point sources in the 2FGL within 20° of 4C +49.22 (source region) including 4C +49.22 itself. The sources within the 10° radius of ROI were fitted with a power-law flux density distribution with photon indices Γ frozen to the values obtained from the likelihood analysis of the full data set, while those beyond 10° ROI radius had both index Γ and normalization frozen to those found in the 2FGL catalogue.

A Galactic diffuse emission model (gal_2yearp7v6_v0.fits) and Isotropic component (iso_p7v6source.txt) were used to model the background.[3]

For the light-curve extraction, which is presented in Section 6, the upper limits (UL) at 2σ confidence level were computed for time intervals in which the likelihood test statistic (Mattox et al. 1996) was less than 9 or the number of model predicted γ rays for 4C +49.22 $N_{pred} < 3$ or $\Delta F(E)/F(E) > 0.5$. The UL estimation procedures are described in the 2FGL catalogue paper (Nolan et al. 2012).

Details on the unbinned likelihood spectra fit for 4C +49.22 in the 0.1–100 GeV range are reported in Table 1 and SED data points for

---

[1] For documentation of the Science Tools, see http://fermi.gsfc.nasa.gov/ssc/data/analysis/documentation/.

[2] http://www.slac.stanford.edu/exp/glast/groups/canda/lat_Performance.htm.

[3] Details on the background model are available from the *Fermi* Science Support Center, see: http://fermi.gsfc.nasa.gov/ssc/data/access/lat/BackgroundModels.html.

Table 1. Summary of the unbinned likelihood spectral fit above 100 MeV.

Interval	Best-fitting model and parameters
Integrated data 2008-08-08 (MJD: 54686) 2011-08-04 (MJD: 55777)	Power law $\Gamma = 2.26 \pm 0.04$ $F_{E > 100\,\mathrm{MeV}} = (5.8 \pm 0.3) \times 10^{-8}$ (ph cm^{-2} s^{-1})
Outburst/high state 2011-05-14 (MJD: 55695) 2011-05-16 (MJD: 55697)	Power law $\Gamma = 2.20 \pm 0.09$ $F_{E > 100\,\mathrm{MeV}} = (1.5 \pm 0.2) \times 10^{-6}$ (ph cm^{-2} s^{-1})
Post-flare/lower state 2011-05-17 (MJD: 55698) 2011-05-26 (MJD: 55707)	Power law $\Gamma = 2.23 \pm 0.08$ $F_{E > 100\,\mathrm{MeV}} = (6.4 \pm 0.6) \times 10^{-7}$ (ph cm^{-2} s^{-1})

Table 2. *Fermi*-LAT SED data points.

Epoch	Frequency (Hz)	$\nu f(\nu)$ (erg cm^{-2} s^{-1})
2011-05-15 (MJD: 55696)	$(6.0 \pm 0.3) \times 10^{22}$ $(2.4 \pm 0.3) \times 10^{23}$ $(9.5 \pm 0.3) \times 10^{23}$ $(3.8 \pm 0.3) \times 10^{24}$	$(2.5 \pm 0.3) \times 10^{-10}$ $(2.2 \pm 0.3) \times 10^{-10}$ $(1.4 \pm 0.4) \times 10^{-10}$ $(8.3 \pm 5.9) \times 10^{-11}$
2011-05-17/25 (MJD: 556978/55706)	$(6.0 \pm 0.3) \times 10^{22}$ $(2.4 \pm 0.3) \times 10^{23}$ $(9.5 \pm 0.3) \times 10^{23}$ $(3.8 \pm 0.3) \times 10^{24}$	$(1.1 \pm 0.1) \times 10^{-10}$ $(8.6 \pm 1.3) \times 10^{-11}$ $(6.4 \pm 1.7) \times 10^{-11}$ $(4.9 \pm 2.8) \times 10^{-11}$

both epochs are reported in Table 2. The estimated systematic uncertainty of the integral fluxes above 100 MeV is about 8.1 per cent and -6.9 per cent for a soft source like 4C +49.22 (Ackermann et al. 2012); the stated uncertainties in the fluxes are statistical only.

3 SIMULTANEOUS MM OBSERVATIONS AND RESULTS BY *Planck*

Planck (Tauber et al. 2010; Planck Collaboration I 2011; Planck Collaboration I 2014) is the third generation space mission to measure the anisotropy of the CMB. It observes the sky in nine frequency bands covering 30–857 GHz with high sensitivity and angular resolution from 31 to 5 arcmin. Full sky coverage is attained in ∼7 months. The Low Frequency Instrument (LFI; Mandolesi et al. 2010; Mennella et al. 2011; Zacchei et al. 2011) covers the 30, 44 and 70 GHz bands with amplifiers cooled to 20 K. The High Frequency Instrument (HFI; Planck HFI Core Team 2011; Planck Collaboration VI 2014) covers the 100, 143, 217, 353, 545 and 857 GHz bands with bolometers cooled to 0.1 K. Polarization is measured in all but the highest two bands (Leahy et al. 2010; Rosset et al. 2010). A combination of radiative cooling and three mechanical coolers produces the temperatures needed for the detectors and optics (Planck Collaboration II 2011). Two Data Processing Centers (DPCs) check and calibrate the data and make maps of the sky (Planck HFI Core Team 2011b; Zacchei et al. 2011). *Planck*'s sensitivity, angular resolution and frequency coverage make it a powerful instrument for Galactic and extragalactic astrophysics as well as cosmology. The *Planck* beams scan the entire sky exactly twice in 1 yr, but scan only about 95 per cent of the sky in six months. For convenience, we call an approximately six month period a 'survey', and use it as a shorthand for one coverage of the sky. In order to take advantage of the simultaneity between the *Planck* observations and the *Fermi*-LAT γ-ray flare of 2011 May 15, flux densities have been extracted from maps produced using only data

collected during a portion of the *Planck* fourth sky survey (2011 May 11–26). Moreover, for comparison we have also extracted flux densities from separate maps for the first (2009 November 16–26), the second (2010 May 11–26) and the third *Planck* survey (2010 November 16–26). Results are reported in Table 3. The ERCSC (Planck Collaboration VII 2011) and the *Planck* catalogue of Compact Sources (PCCS; Planck Collaboration XXVIII 2014) include average flux densities for 4C +49.22. All of these maps have been produced through the standard LFI and HFI pipelines adopted for the internal DX8 release. LFI flux densities were obtained at 30, 44 and 70 GHz using the IFCAMEX code, an implementation of the Mexican Hat Wavelet 2 (MHW2) algorithm that is being used in the LFI DPC infrastructure to detect and extract flux densities of point-like sources in CMB maps. This wavelet is defined as the fourth derivative of the two-dimensional Gaussian function, where the scale of the filter is optimized to look for the maximum in the signal-to-noise ratio (S/N) of the sources in the filtered map, and has been previously applied to *WMAP* and *Planck* data and simulations (González-Nuevo et al. 2006; López-Caniego et al. 2006, 2007; Massardi et al. 2009). First, we obtained a flat patch centred on the source and applied the MHW2 software. This algorithm produces an unbiased estimation of the flux density of the source and its error. Secondly, we convert the peak flux density from temperature units to Jy sr^{-1} and then to Jy by multiplying it by the area of the instrument beam, taking the beam solid angle into account. In this analysis, we used the effective Gaussian FWHM whose area is that of the actual elliptical beam at 30, 44 and 70 GHz, respectively, as provided by the LFI DPC. HFI flux densities have been extracted using aperture photometry. Flux densities were evaluated assuming a circularly symmetric Gaussian beam of the given FWHM. An aperture is centred on the position of the source and an annulus around this aperture is used to evaluate the background. A correction factor which accounts for the flux of the source in the annulus may be calculated and is given below, where k_0, k_1 and k_2 are the number of FWHMs of the radius of the aperture, the inner radius of the annulus and the outer radius of the annulus, respectively.

$$F_{\mathrm{true}} = \left(1 - \left(\frac{1}{2} \right)^{4k_0^2} - \left(\left(\frac{1}{2} \right)^{4k_1^2} - \left(\frac{1}{2} \right)^{4k_2^2} \right) \frac{k_0^2}{k_2^2 - k_1^2} \right)^{-1}$$
$$\times F_{\mathrm{obs}}. \tag{1}$$

Here, we used a radius of 1 FWHM for the aperture, $k_0 = 1$; the annulus is located immediately outside of the aperture and has a width of 1 FWHM, $k_1 = 1$ and $k_2 = 2$. The flux density, F_{true} may then be evaluated from the observed flux density, F_{obs}, where F_{obs} is the total flux inside the aperture after the background has been subtracted. *Planck* data for each survey are reported in Table 3.

Table 3. Flux densities for 4C +49.22 from the four *Planck* surveys. First survey: 2009 November 16–26, second survey: 2010 May 11–26, third survey: 2010 November 16–26, fourth survey: 2011 May 11–26.

Planck-LFI survey	ν (GHz)	Flux density (Jy)	Errors (Jy)
First	30	1.14	0.15
Second	30	1.66	0.12
Third	30	1.75	0.14
Fourth	30	1.46	0.13
First	44	1.24	0.26
Second	44	1.93	0.24
Third	44	1.28	0.26
Fourth	44	1.95	0.13
First	70	1.21	0.13
Second	70	1.85	0.18
Third	70	1.40	0.23
Fourth	70	2.36	0.16

Planck-HFI survey	ν (GHz)	Flux density (Jy)	Errors (Jy)
First	100	0.57	0.23
Second	100	1.93	0.15
Third	100	1.58	0.17
Fourth	100	2.37	0.17
First	143	0.51	0.20
Second	143	1.62	0.16
Third	143	1.58	0.18
Fourth	143	2.26	0.15
First	217	0.41	0.10
Second	217	1.48	0.11
Third	217	1.30	0.08
Fourth	217	1.98	0.09
First	353	0.42	0.20
Second	353	0.98	0.09
Third	353	1.04	0.12
Fourth	353	1.61	0.09
First	545	0.20	0.21
Second	545	0.76	0.17
Third	545	0.72	0.18
Fourth	545	1.34	0.20
First	857	0.25	UL
Second	857	0.17	0.23
Third	857	0.32	0.27
Fourth	857	0.74	0.20

Spectra presented in Fig. 1 are modelled with a broken power law; see equation 5 of León-Tavares et al. (2012), in order to characterize the evolution of the sub-mm spectra in terms of the spectral classification presented in Fig. 2 of León-Tavares et al. (2012). Within the mentioned classification scheme the hard sub-mm spectrum observed during 2009 November (open circles) can be classified as spectral-type A (both power-law indices, $\alpha_{mm} < 0$, $\alpha_{sub-mm} < 0$ and the relative difference between indices is less than 50 per cent), thus indicating the absence of a new jet component in a very early development stage. As the plasma blob propagates down the jet, the shape of the spectrum changes; the relative difference between α_{mm} and α_{sub-mm} became greater than 50 per cent as can be seen in 2010 May and 2010 November, respectively. These spectral shapes can be classified as spectral-type C. As the plasma blob propagates down the jet, its spectral turnover shifts to lower frequencies, from 170 GHz of 2010 May and 2010 November to around 100 GHz in 2011 May. The sub-mm spectrum of 2011 May, simultaneous to
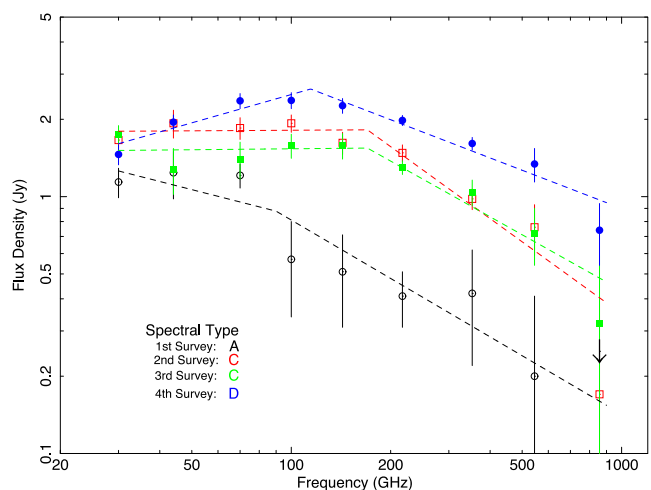

Figure 1. *Planck* flux densities for 4C +49.22 at all nine frequencies as reported in Table 3. Each frequency is shown in four colours corresponding to four surveys: black open circles correspond to the first survey, red open squares to the second, green filled squares to the third and blue filled circle to the fourth.

the γ-ray flare, shows a well-defined synchrotron component and it is consistent with spectral-type D ($\alpha_{mm} > 0$ and $\alpha_{sub-mm} < 0$). Sources with sub-mm spectra classified as spectral type C or D are more likely to be strong γ-ray emitters, which is in good agreement with the fact that 4C +49.22 became a γ-ray emitter only after its sub-mm spectral shape changed to spectral-type D (León-Tavares et al. 2012). This spectral shape can be associated with a single synchrotron component that becomes self-absorbed in the middle of the mm wavelength regime. Such high spectral turnover frequencies reveal the presence of emerging disturbances in the jet that are likely to be responsible for the high levels of γ-ray emission (Marscher 2006, 2014).

4 SIMULTANEOUS X-RAY AND UV–OPTICAL OBSERVATIONS AND RESULTS FROM *Swift*

In response to the high γ-ray activity of 4C +49.22, the *Swift* satellite (Gehrels et al. 2004) performed nine ToO observations, between 2011 April 26 and May 25. In order to reference the source's past activity, we also analysed the observations performed on 2008 April 8, 2009 May 6 and 2009 May 17. The 2011 observations were performed using two of three on-board instruments: the XRT (Burrows et al. 2005, 0.2–10.0 keV) and the UltraViolet Optical Telescope (UVOT; Roming et al. 2005b, 170–600 nm). The archival data from the Burst Alert Telescope (BAT; Barthelmy et al. 2005, 15–150 keV) from Cusumano et al. (2010b) and Cusumano et al. (2010a) were added to the SEDs as reference of the low state.

The XRT data were reprocessed with standard procedures (XRT-PIPELINE v0.12.6), filtering and screening criteria by using the HEA-SOFT package (v6.10). We considered data collected using the photon counting mode with XRT event grades between 0 and 12. Since the source count rate was always below 0.5 counts s^{-1} no pile-up correction was necessary. Source events were extracted from a circular region with a radius of 20 pixels (1 pixel $\sim$ 2.36 arcsec), while background events were extracted from a circular region with a radius of 50 pixels, away from background sources. Ancillary response files were generated with XRTMKARF, and account for different extraction regions, vignetting and PSF corrections. We used the spectral
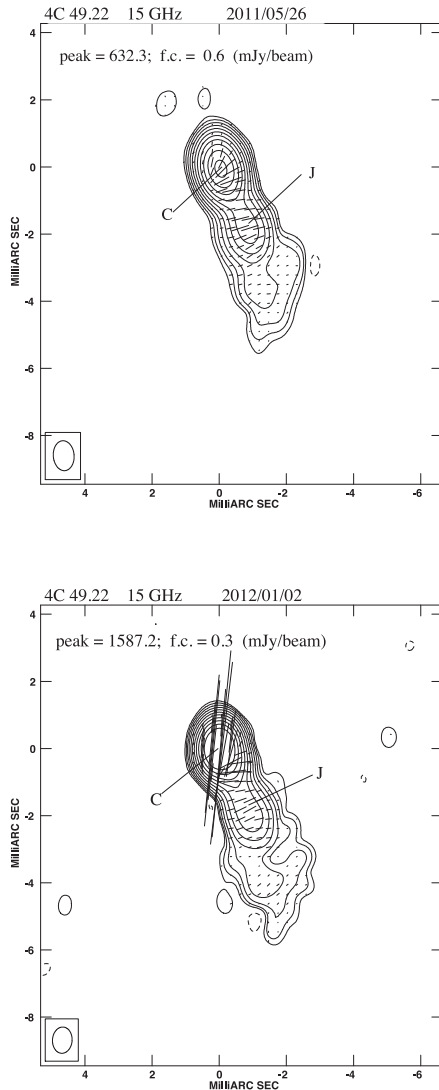
Figure 2. 15-GHz VLBA images of 4C +49.22 from the observations on 2011 May (upper panel) and 2012 January (bottom panel). On each image, we provide the observing date. The peak flux density is in mJy beam^{-1} and the first contour (f.c.) intensity is in mJy beam^{-1}, which corresponds to three times the off-source noise level. Contour levels increase by a factor of 2. The restoring beam is plotted in the bottom left-hand corner. The vectors superimposed on the total intensity flux density contours show the position angle of the electric vector, where 1 mm length corresponds to 7.1 mJy beam^{-1}.

redistribution matrices v011 in the calibration data base maintained by HEASARC.[4]

All spectra were rebinned with a minimum of 20 counts per energy bin to allow χ^2 fitting within XSPEC (v12.6.0). We fit the individual spectra with a simple absorbed power law, with a neutral hydrogen column fixed to its Galactic value (2.13×10^{20} cm^{-2}; Kalberla et al. 2005). In addition, we summed the data collected after the γ-ray flare (2011 May 17–25) in order to have better statistics see SED figures in Section 7. The fit results are reported in Table 4 and the SED data points are reported in Table 5. During the nine ToOs performed in 2011 April–May, *Swift*-XRT observed a 0.3–10 keV flux in the range (0.8–2.1) × 10^{-11} erg cm^{-2} s^{-1}, a

[4] http://heasarc.gsfc.nasa.gov/

factor between 2 and 5 higher than the flux level observed in 2008–2009. This is a hint that the mechanism that produced an increase of the activity observed in γ-rays also affected the X-ray part of the spectrum.

The peak of the X-ray flux was detected on 2011 May 15, soon after the major γ-ray flare was detected by *Fermi*-LAT. The flare X-ray spectrum was softer than that of the post-flare epoch, thus demonstrating the contribution of the synchrotron component to lower energy X-ray emission. This implies a shift of the synchrotron and IC peaks towards higher energies on May 15.

The *Swift*-UVOT can acquire images in six lenticular filters (*V*, *B*, *U*, *UVW*1, *UVM*2 and *UVW*2, with central wavelengths in the range 170–600 nm). After 7 yr of operations, observations are now carried out using only one of the filters unless specifically requested by the user. Therefore, images are not always available for all filters in all the observations. The log of *Swift*-UVOT observations analysed is reported in Table 6.

The photometry analysis of all the 4C +49.22 observations was performed using the standard UVOT software distributed within the HEASOFT 6.9.0 package and the calibration included in the most recent release of the 'Calibration Database'.

We extracted source counts using a standard circular aperture with a 5 arcsec radius for all filters, and the background counts using an annular aperture with an inner radius of 26 arcsec and a width of 8 arcsec. Source counts were converted to fluxes using the task UVOTSOURCE and the standard zero-points (Poole et al. 2008). Fluxes were then de-reddened using the appropriate values of $E(B - V)$ for the source taken from Schlegel, Finkbeiner & Davis (1998) and the $A_\lambda/E(B - V)$ ratios calculated for UVOT filters using the mean Galactic interstellar extinction curve from Fitzpatrick (1999).

Using *U*-band filter images only, we detected variability within a single exposure (a few hours time-scale) in the flare observation of 2011 May 15. We show in Fig. 3 the *U*-band flux variation within this observation. If we compare the first 'segment' of the exposure to the last, the variation is about 7σ. This last segment is the shortest (34 s), and has the largest flux error. Intraday variability in a single observation has been detected also on May 19 in *U*, and on May 22 in *M*2 filters. The May 19 observation includes three segments and shows a flux increase on the last one (1230 s), while on May 22 the third (191 s) of four segments shows a lower flux. The May 19 episode is the most significant, with an ∼10σ variation.

5 GROUND BASED AND LONGER TERM RADIO–OPTICAL OBSERVATIONS

5.1 MOJAVE monitoring and component motion studies

In order to study the parsec-scale morphology and possible changes in the source structure, we analysed 13-epoch VLBA observations at 15 GHz from the MOJAVE programme[5] spanning a time interval from 2008 May to 2013 February. We imported the calibrated *uv* data sets (Lister et al. 2009) into the NRAO AIPS package and performed a few phase-only self-calibration iterations before producing the final total intensity images. Uncertainties on the flux density scale are within 5 per cent (Lister et al. 2013). For the six data sets obtained after the γ-ray flare, we also produced Stokes' *Q* and *U* images to study possible variations of the source polarization.

[5] The MOJAVE data archive is maintained at http://www.physics.purdue.edu/MOJAVE.

Table 4. Log and fitting results of the data obtained by the XRT instrument on board *Swift*.

Date	Exp. time (s)	Photon index	Unabsorbed flux 0.3–10 keV (erg cm^{-2} s^{-1})	$\chi 2_{\mathrm{red}}$ (d.o.f.)
2008-04-28 (MJD: 54584)	5438	1.82 ± 0.11	$(4.8 \pm 0.4) \times 10^{-12}$	0.83 (24)
2009-05-06 (MJD: 54957)	3122	1.80 ± 0.16	$(3.8 \pm 0.5) \times 10^{-12}$	0.64 (10)
2009-11-17 (MJD: 55152)	5218	2.05 ± 0.14	$(3.8 \pm 0.4) \times 10^{-12}$	0.71 (17)
2011-04-26 (MJD: 55677)	4647	1.99 ± 0.08	$(1.1 \pm 0.1) \times 10^{-11}$	0.75 (44)
2011-04-29 (MJD: 55680)	4813	1.69 ± 0.10	$(7.8 \pm 0.6) \times 10^{-12}$	0.91 (32)
2011-05-02 (MJD: 55683)	4396	1.77 ± 0.11	$(7.6 \pm 0.6) \times 10^{-12}$	1.10 (27)
2011-05-15 (MJD: 55696)	3611	2.03 ± 0.06	$(2.1 \pm 0.1) \times 10^{-11}$	0.79 (77)
2011-05-17 (MJD: 55698)	3406	1.70 ± 0.08	$(1.2 \pm 0.1) \times 10^{-11}$	0.75 (36)
2011-05-19 (MJD: 55700)	3708	1.87 ± 0.08	$(1.2 \pm 0.1) \times 10^{-11}$	0.92 (42)
2011-05-22 (MJD: 55703)	4141	1.74 ± 0.09	$(8.4 \pm 0.6) \times 10^{-12}$	0.73 (32)
2011-05-23 (MJD: 55704)	4002	1.69 ± 0.09	$(9.3 \pm 0.7) \times 10^{-12}$	0.86 (31)
2011-05-25 (MJD: 55706)	3920	1.70 ± 0.10	$(8.8 \pm 0.7) \times 10^{-12}$	1.03 (31)
2011-05-17/25 (MJD: 55698/55706)	19176	1.76 ± 0.04	$(1.1 \pm 0.1) \times 10^{-11}$	0.93 (152)

Table 5. *Swift*-XRT SED data points.

Epoch	Frequency (Hz)	$\nu f(\nu)$ (erg cm^{-2} s^{-1})
2011-05-15 (MJD: 55696)	9.1×10^{16}	$(6.5 \pm 0.4) \times 10^{-12}$
	1.4×10^{17}	$(6.1 \pm 0.4) \times 10^{-12}$
	1.9×10^{17}	$(6.8 \pm 0.4) \times 10^{-12}$
	2.5×10^{17}	$(6.0 \pm 0.4) \times 10^{-12}$
	3.2×10^{17}	$(6.9 \pm 0.5) \times 10^{-12}$
	3.9×10^{17}	$(5.9 \pm 0.4) \times 10^{-12}$
	5.6×10^{17}	$(6.4 \pm 0.4) \times 10^{-12}$
	9.5×10^{17}	$(6.3 \pm 0.4) \times 10^{-12}$
	1.6×10^{18}	$(6.5 \pm 1.5) \times 10^{-12}$
2011-05-17/25 (MJD: 55698/55706)	8.8×10^{16}	$(2.1 \pm 0.1) \times 10^{-12}$
	1.3×10^{17}	$(2.2 \pm 0.1) \times 10^{-12}$
	1.7×10^{17}	$(2.4 \pm 0.1) \times 10^{-12}$
	2.1×10^{17}	$(2.5 \pm 0.1) \times 10^{-12}$
	2.5×10^{17}	$(2.8 \pm 0.2) \times 10^{-12}$
	2.9×10^{17}	$(2.7 \pm 0.1) \times 10^{-12}$
	3.4×10^{17}	$(2.8 \pm 0.1) \times 10^{-12}$
	4.1×10^{17}	$(3.0 \pm 0.2) \times 10^{-12}$
	4.9×10^{17}	$(3.1 \pm 0.2) \times 10^{-12}$
	6.1×10^{17}	$(3.3 \pm 0.2) \times 10^{-12}$
	7.8×10^{17}	$(3.7 \pm 0.2) \times 10^{-12}$
	1.0×10^{18}	$(3.9 \pm 0.2) \times 10^{-12}$
	1.5×10^{17}	$(4.1 \pm 0.3) \times 10^{-12}$

The uncertainties on the polarization angle are less than 5° (Lister et al. 2013).

The source 4C +49.22 shows a one-sided core-jet structure that is 6 mas in size (i.e. ∼28 pc at the source redshift) and the radio emission is dominated by the core component, labelled C in Fig. 2. Following a detection of the γ-ray flare on 2011 May 15, the core component of this source showed an increase in both the total intensity of emission and the polarization percentage, while the polarization angle has rotated by about 60°. On the other hand, no significant changes have been found in the jet structure, labelled J in Fig. 2, strongly suggesting that the region responsible for the radio variability is located within the central component. Total intensity flux density and polarization properties of the core and jet components are reported in Table 7.

The total intensity and polarization flux densities were measured on the image plane with the Astronomical Image Processing Sys-

tem (AIPS)[6] using the Gaussian-profile fitting task JMFIT and the task TVSTAT, which performs an aperture integration on a selected region. As the source core we consider the unresolved central component, and we derive its parameters with JMFIT. The jet is the remaining structure, and the parameters are obtained by subtracting the core contribution to the total emission measured by TVSTAT. Errors are computed using the formulas from Fanti et al. (2001).

To derive structural changes, in addition to the analysis performed on the image plane, we also fitted the visibility data with circular Gaussian components at each epoch using the model-fitting option in DIFMAP. Errors Δr associated with the component position are estimated by means of $\Delta r = a/(S_{\mathrm{p}}/\mathrm{rms})$, where a is the component deconvolved major-axis, S_{p} is its peak flux density and rms is the 1σ noise level measured on the image plane (Orienti et al. 2011). In case the errors estimated are unreliably small, we assume a more conservative value for Δr that is 10 per cent of the beam.

This approach is preferable in order to derive small variations in the source structure; it also provides a more accurate fit of unresolved structures close to the core component.

Throughout the observing epochs we could reliably follow the motion of only two components, labelled J1 and J2 in Fig. 4; a third component, J3, became visible in the last seven epochs. Interestingly, a new component, J4, was detected in the last three epochs of MOJAVE data, since 2012 August. We determined the separation velocity from the core, considered stationary, for these four components by means of a linear regression fit that minimizes the chi-square error statistics (Fig. 5). From this analysis, we found that J1, J2, J3 and J4 are increasing their separation from the core with apparent angular velocities of 0.48 ± 0.01, 0.27 ± 0.01, 0.30 ± 0.02 and 0.27 ± 0.09 mas yr^{-1}, which correspond to apparent linear velocities $\beta_{\mathrm{app}} = v_{\mathrm{app}}/c$ of 9.9 ± 0.2, 5.6 ± 0.2, 6.2 ± 0.4 and 5.6 ± 1.4, respectively. The velocity derived for J1 is in agreement with the value found by Lister et al. (2013), while for J2 we obtain a slower speed. This may be due to a deceleration that may become detectable with the availability of additional observing epochs not considered in Lister et al. (2013). The large uncertainty on the velocity of component J4 is due to the availability of only three observing epochs spanning a very short time interval of about seven months. From a linear regression fit we estimated the time of zero separation, which provides an indication of the ejection epoch. We found that

---

[6] http://www.aips.nrao.edu

Table 6. Log of the data obtained by the UVOT instrument on board *Swift*. All magnitudes are corrected for Galactic extinction.

Date	Exp. time (s)	*V* (mag)	*B* (mag)	*U* (mag)	*W*1 (mag)	*M*2 (mag)	*W*2 (mag)
2008-04-28 (MJD: 54584)	5398	–	–	–	15.64 ± 0.04	–	–
2009-05-06 (MJD: 54957)	2980	17.62 ± 0.09	17.59 ± 0.05	16.40 ± 0.04	16.42 ± 0.05	15.91 ± 0.05	16.06 ± 0.04
2009-11-17 (MJD: 55152)	5034	17.34 ± 0.07	17.18 ± 0.04	16.01 ± 0.03	15.72 ± 0.04	15.28 ± 0.04	15.41 ± 0.03
2011-04-26 (MJD: 55677)	1336	–	–	–	14.77 ± 0.04	–	–
2011-04-29 (MJD: 55680)	4750	16.37 ± 0.04	16.55 ± 0.04	15.55 ± 0.04	15.42 ± 0.04	15.10 ± 0.04	15.22 ± 0.04
2011-05-02 (MJD: 55683)	4247	15.97 ± 0.04	16.27 ± 0.04	15.21 ± 0.04	15.12 ± 0.04	14.82 ± 0.04	14.96 ± 0.04
2011-05-15 (MJD: 55696)	3592	–	–	14.14 ± 0.02	–	–	–
2011-05-17 (MJD: 55698)	3390	15.50 ± 0.03	15.70 ± 0.02	14.79 ± 0.02	14.73 ± 0.03	14.56 ± 0.04	14.70 ± 0.03
2011-05-19 (MJD: 55700)	3689	–	–	14.25 ± 0.02	–	–	–
2011-05-22 (MJD: 55703)	4077	–	–	–	15.14 ± 0.03	14.87 ± 0.03	15.04 ± 0.03
2011-05-23 (MJD: 55704)	3936	–	–	–	14.70 ± 0.03	14.47 ± 0.03	14.63 ± 0.03
2011-05-25 (MJD: 55706)	3849	–	–	–	15.28 ± 0.03	14.97 ± 0.03	15.15 ± 0.03
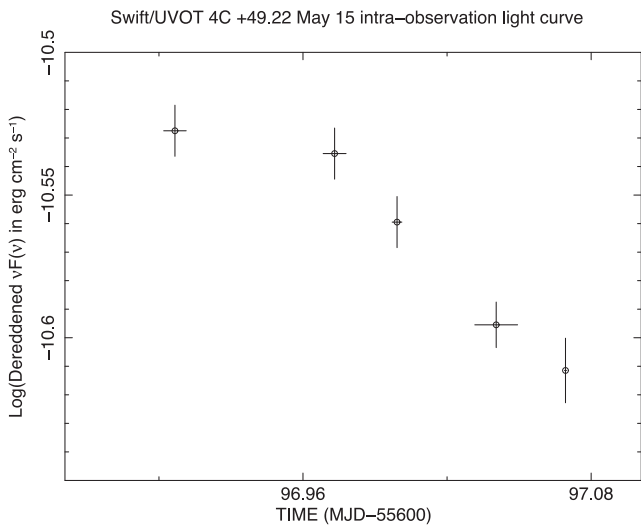
Figure 3. Photometric *U*-band intraday light curve obtained by *Swift*-UVOT in 2011 May 15.

J4 emerged from the core on 2011.52 (i.e. beginning of July 2011), making the ejection of the component close in time to the γ-ray flare. However, the large uncertainties on the separation velocity do not allow us to accurately constrain the precise time of zero separation, which ranges between 2010.73 (i.e. 2010 September) and 2011.92 (i.e. 2011 December). It is worth noting that the time of zero separation estimated for component J3 is 2010.3 ± 0.2 (i.e. 2010 April) with an associated uncertainty on the ejection time that

ranges between 2010 February and June. Interestingly, no strong γ-ray flare was reported close in time with the ejection of this component, but the source turned out to be repeatedly detectable by LAT on a weekly time-scale after 2010 February (see Section 6). By means of the apparent velocities derived for the jet components, we estimated the possible combination of the intrinsic velocity $\beta = v/c$ and the angle θ that the jet forms with our line of sight:

$$\beta_{\mathrm{app}} = \frac{\beta \sin\theta}{1 - \beta\cos\theta}. \tag{2}$$

We assumed that β_{app} is between 9.9 and 5.6, i.e. the velocity estimated for the fastest and slowest components. In the former case, we found that $\beta > 0.995$ and $\theta < 11°$, while in the latter $\beta > 0.985$ and $\theta < 20°$. Another way to derive the possible (β–θ) combinations is using the flux density ratio of the approaching, S_a, and receding S_r jets:

$$\frac{S_a}{S_r} = \left(\frac{1 + \beta\cos\theta}{1 - \beta\cos\theta} \right)^{3+\alpha}, \tag{3}$$

where α is the spectral index ($S_\nu \propto \nu^{-\alpha}$), and it is assumed to be 0.7, i.e. a typical value for the jet component. From the lack of detection of a counterjet in any of the images, we set a lower limit on the jet/counterjet ratio. We used the highest ratio between the jet and counterjet emission, which is computed by using $S_a = 816$ mJy (i.e. the flux density of J4 as it emerges from the core, see Table 7), and $S_r = 0.3$ mJy, which corresponds to 1σ rms. From these values we derive a jet/counterjet ratio >2720. This value yields $\beta\cos\theta > 0.79$ c, implying $\beta > 0.79$ and $\theta < 38°$, which are consistent with the range found from equation (2).

Table 7. Total intensity flux density and polarization properties. Column 1: observing date; Cols. 2, and 3: total intensity flux density of component C and J, respectively; Cols. 4, and 5: polarized flux density (and polarization percentage) for component C and J, respectively; Cols. 6, and 7: polarization angle for component C and J, respectively.

Date	S_C (mJy)	S_J (mJy)	$S_{\mathrm{pol, C}}$ (mJy, per cent)	$S_{\mathrm{pol, J}}$ (mJy, per cent)	χ_C (deg)	χ_J (deg)
2011-05-26 (MJD: 55707)	658 ± 33	88 ± 5	5.8 ± 0.5 (0.9 ± 0.1 per cent)	7.2 ± 0.7 (8.1 ± 0.8 per cent)	-64 ± 5	-66 ± 5
2011-08-15 (MJD: 55788)	947 ± 47	91 ± 5	9.4 ± 0.6 (1.0 ± 0.1 per cent)	7.4 ± 0.7 (8.1 ± 0.8 per cent)	-84 ± 5	-77 ± 5
2012-01-02 (MJD: 55928)	1708 ± 85	87 ± 4	45.1 ± 2.2 (2.6 ± 0.1 per cent)	8.2 ± 0.8 (9.4 ± 0.8 per cent)	-10 ± 5	-73 ± 5
2012-08-03 (MJD: 56142)	1650 ± 82	92 ± 5	59.0 ± 3.0 (3.5 ± 0.2 per cent)	6.0 ± 0.7 (6.5 ± 0.7 per cent)	10 ± 5	-62 ± 5
2012-11-11 (MJD: 56242)	1381 ± 69	63 ± 3	62.0 ± 3.1 (4.5 ± 0.2 per cent)	5.0 ± 0.6 (7.9 ± 0.9 per cent)	19 ± 5	-67 ± 5
2013-02-28 (MJD: 56351)	1081 ± 54	65 ± 3	20.0 ± 1.1 (1.9 ± 0.1 per cent)	6.0 ± 0.7 (9.2 ± 1.0 per cent)	48 ± 5	-70 ± 5

4C 49.22   15 GHz   2013/02/28

peak = 651.0; f.c. = 3.0 (mJy/beam)
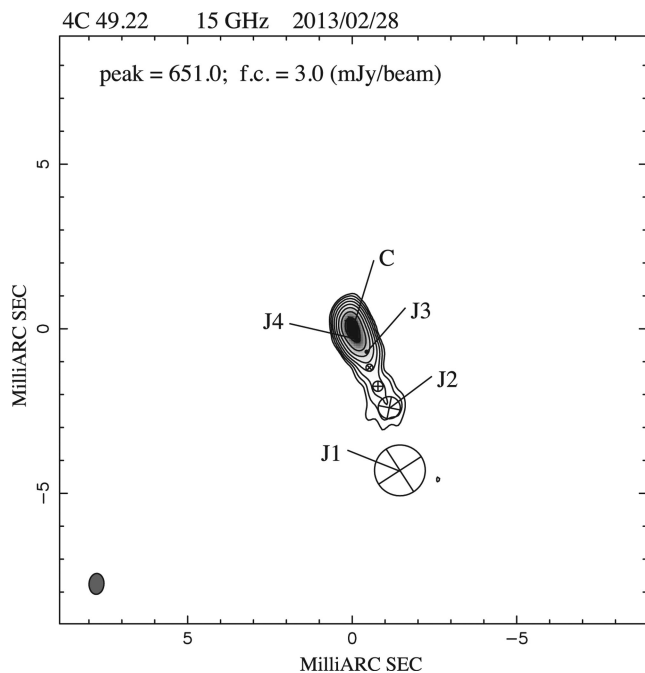
Figure 4. 15-GHz VLBA image from the observations performed during 2013 February with the positions of the jet components discussed in Section 5.1. The peak flux density is in mJy beam^{-1} and the first contour (f.c.) intensity is in mJy beam^{-1}, and it corresponds to 0.5 per cent of the peak flux density. Contour levels increase by a factor of 2. The restoring beam is plotted in the bottom left-hand corner.
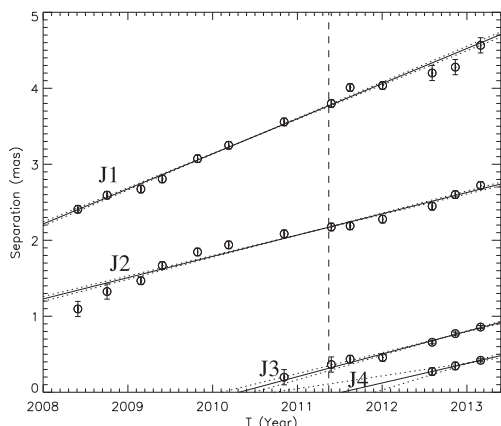
Figure 5. Changes in separation with time between component C, considered stationary, and J1, J2, J3 and J4. The solid lines represent the linear fits to the data, while the dotted lines represent the uncertainties from the fit parameters. The vertical dashed line indicates the time of the γ-ray flare.

With the derived values we can compute a lower limit on the Doppler factor by means of

$$\mathcal{D} = \frac{1}{\Gamma(1 - \beta\cos\theta)}, \quad (4)$$

where Γ is the bulk Lorentz factor. The lower limit on the Doppler factor is $\mathcal{D} > 4.2$, which is compatible with those derived from our SED modelling (see Section 7). However, this estimate is affected by the large uncertainties in the apparent velocity and more observations spanning a larger time interval with frequent time sampling are necessary. Our SED modelling results (Section 7) are constrained to

$\mathcal{D}$ values between ~20 and ~30, maintaining therefore the agreement with variability Doppler factors obtained recently for a sample of *Fermi*-LAT blazars (e.g. Pushkarev et al. 2009; Savolainen et al. 2010), and in particular maintaining the agreement with previous SED modelling of 4C +49.22 (Sambruna et al. 2006b). The observed increasing flux density and polarization degree in the radio core of 4C +49.22 after the GeV γ-ray flare demonstrate that the high-energy peak emission is produced in or close to the radio core rather than in structures and blobs at larger distance along the jet, far from the central engine.

Even if this does not yet constrain the flaring GeV emission region (sometimes called the 'blazar zone') to within the BLR, we can at least exclude flaring GeV emission produced by jet knots placed at a large distance from the central engine (e.g. few parsecs Lister et al. 2013). This result can help to discriminate between our multi-temporal and MW SED modelling described in Section 7.

5.2 Metsähovi Radio Observatory

Observations at 37 GHz were made with the 13.7-m diameter Metsähovi radio telescope, which is a radome-enclosed paraboloid antenna situated in Finland. The measurements were made with a 1 GHz-band dual beam receiver centred at 36.8 GHz. The observations are ON–ON observations, alternating the source and the sky in each feed horn. A typical integration time to obtain one flux density data point is between 1200 and 1400 s. The detection limit of the telescope at 37 GHz is of the order of 0.2 Jy under optimal conditions. Data points with an S/N < 4 are handled as non-detections. The flux density scale is set by observations of DR 21. Sources NGC 7027, M87 (3C 274) and NGC 1275 (Per A, 3C 84) are used as secondary calibrators. A detailed description of the data reduction and analysis is given in Teräsranta et al. (1998). The error estimate in the flux density includes the contribution from the measurement rms and the uncertainty of the absolute calibration. The flux density light curve is shown in Fig. 6 and Table 8.

5.3 Quasi-simultaneous near-infrared monitoring by INAOE

The near-infrared (NIR) photometry was performed in J, K_s and H band with the CAnanea Near Infrared CAmera (CANICA) NIR camera at the 2.1-m telescope of the Observatorio Astrofísico Guillermo Haro (OAGH) in Cananea, Sonora, Mexico. CANICA is a camera based on a HAWAII 1024 × 1024 pixel array, with plate scale and field of view 0.32 arcsec pixel^{-1} and about 5.5 × 5.5 arcmin^2, respectively. Observations were reduced using standard differential aperture photometry with IRAF packages.[7] Every night, several standard stars from Hunt et al. (1998) were observed in both bands. The photometric error for each night was assumed to be the standard deviation between our estimated magnitude and the magnitude determined in Hunt et al. (1998) for the standard stars observed. The mean zero-point error in J and H in the photometric nights is 0.06 mag, reaching 0.08 mag on the photometric nights. Similarly, in K_s we have errors of 0.08 and 0.10 mag, respectively. As expected, the error estimates show that the photometric accuracy is generally higher in J and H than in K_s. We note that our average errors in the photometric zero-point are 0.07 mag in J and H and 0.09 mag in K_s, which is quite good for NIR bands. The flux densities in the three filters are reported in Fig. 7 and in Table 9.

---

[7] http://iraf.noao.edu/
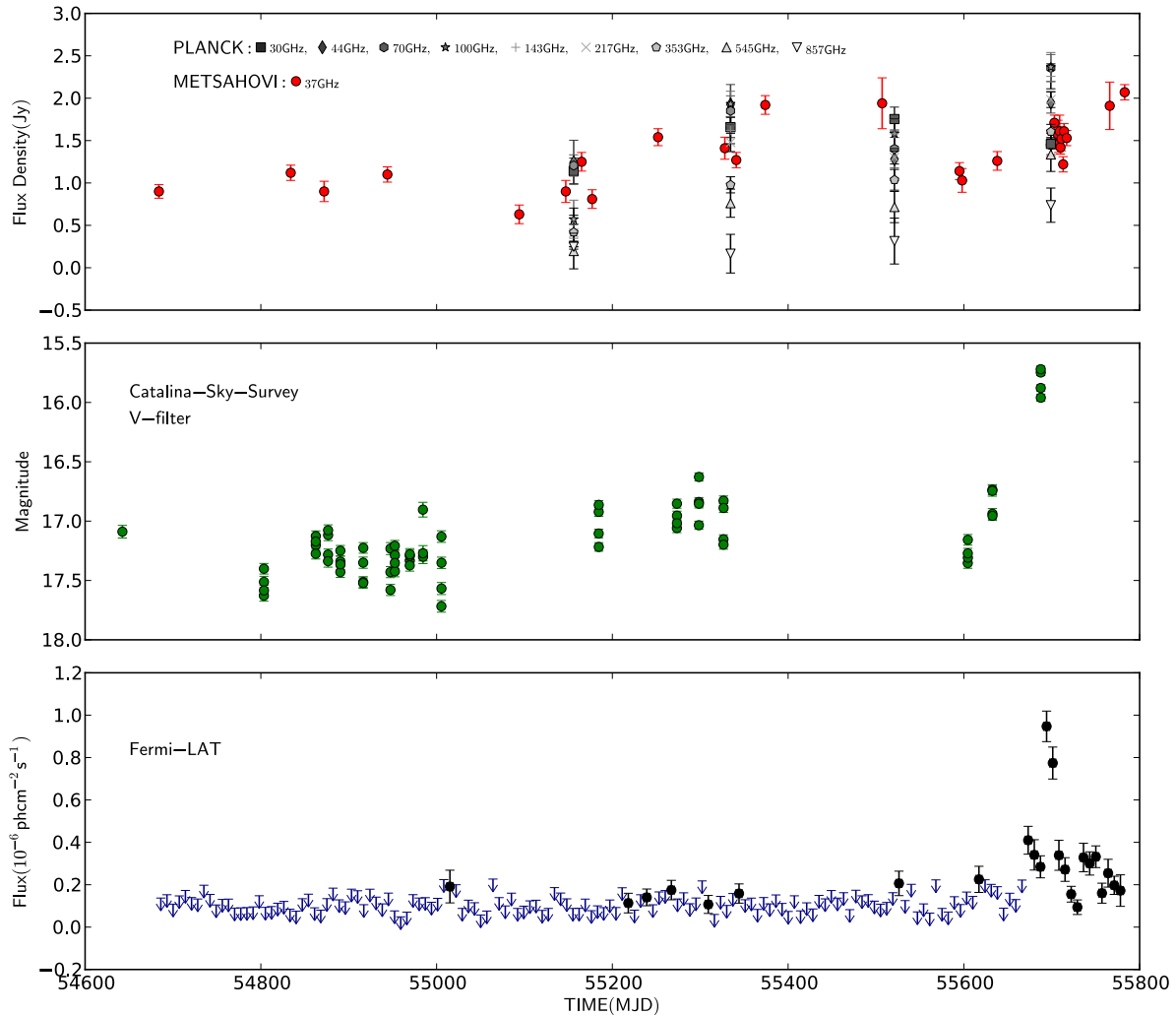
Figure 6. Multifrequency light curves using the long term monitoring data. Top panel: Metsähovi radio data and *Planck* (described in Section 5.2 and in Section 3), middle panel: CSS (described in Section 5.4), bottom panel: 36 months γ-ray integrated flux ($E > 100$ MeV) light curve measured by *Fermi*-LAT from 2008 August 4 to 2011 August 4. The time binning is 7 d: blue arrows represent the 2σ ULs (described in Section 2).

Each image was checked for problems before going through all the data-reduction steps. For the treatment of the images, we used the GEMINI IRAF1 package. Flat-field images were obtained through the QFLAT task from combining many dome images. We decided to use dome flat-fields instead of flat images obtained from sky images; after checking with many standard stars, we discovered that the former produced more accurate results in terms of photometry (i.e. smaller zero-point errors). The QSKY task was used to estimate the background contribution. For each image, the background was estimated from the four sky images closest in time. Furthermore, the mean and standard deviation of each sky image were calculated, and if the mean was discrepant from that of the other three sky images by more than 10 per cent of the standard deviation, then the image was removed from the process. In this way, we avoid background changes and ensure a proper background subtraction. These corrections (flat-fielding and background subtraction) were performed for every galaxy and standard star image by QREDUCE, using the appropriate flat-field and background images. Finally, the IMCOADD task combines all corrected images of a galaxy according to their median, calculating the necessary shifts due to the dither pattern.

5.4 CSS observations

The CSS for near-Earth objects and potential planetary hazard asteroids (Near Earth Object/Potentially Hazardous Asteroids [NEO/PHA]) is conducted by the University of Arizona Lunar and Planetary Laboratory group.[8] CSS utilizes three wide-field telescopes: the 0.68-m Catalina Schmidt at Catalina Station, AZ; the 0.5-m Uppsala Schmidt (Siding Spring Survey, or SSS, in collaboration with the Australian National University) at Siding Spring Observatory, NSW, Australia; and the Mt Lemmon Survey (MLS), a 1.5-m reflector located on Mt Lemmon, AZ. Each telescope employs a camera with a single, cooled, 4k × 4k back-illuminated, unfiltered CCD. Between the three telescopes, the majority of the observable sky is covered at least once (and up to four times) per lunation, depending on the time since the area was last surveyed and its proximity to the ecliptic. The total area coverage is ∼30 000 deg², and it excludes the Galactic plane within $|b| < 10°$. For each coverage four images of the same field are taken, separated in time

[8] S. Larson, E. Beshore, and collaborators; see http://www.lpl.arizona.edu/css/.

Table 8. Flux densities of 4C +49.22 with Metsähovi Radio Observatory at 37 GHz.

Date	Flux density (mJy)
2008-08-06 (MJD: 54684.0)	0.90 ± 0.08
2009-01-03 (MJD: 54834.0)	1.12 ± 0.09
2009-02-10 (MJD: 54872.0)	0.90 ± 0.12
2009-04-23 (MJD: 54944.0)	1.10 ± 0.09
2009-09-20 (MJD: 55094.0)	0.63 ± 0.11
2009-11-12 (MJD: 55147.0)	0.90 ± 0.13
2009-11-30 (MJD: 55165.0)	1.25 ± 0.11
2009-12-12 (MJD: 55177.0)	0.81 ± 0.11
2010-02-25 (MJD: 55252.0)	1.54 ± 0.1
2010-05-12 (MJD: 55328.0)	1.41 ± 0.13
2010-05-25 (MJD: 55341.0)	1.27 ± 0.09
2010-06-27 (MJD: 55374.0)	1.92 ± 0.11
2010-11-07 (MJD: 55507.0)	1.94 ± 0.3
2011-02-03 (MJD: 55595.0)	1.14 ± 0.1
2011-02-06 (MJD: 55598.0)	1.03 ± 0.14
2011-03-18 (MJD: 55638.0)	1.26 ± 0.11
2011-05-18 (MJD: 55699.0)	1.45 ± 0.14
2011-05-22 (MJD: 55703.0)	1.71 ± 0.09
2011-05-26 (MJD: 55707.0)	1.57 ± 0.17
2011-05-27 (MJD: 55708.0)	1.46 ± 0.1
2011-05-28 (MJD: 55709.0)	1.61 ± 0.19
2011-05-29 (MJD: 55710.0)	1.42 ± 0.08
2011-05-30 (MJD: 55711.0)	1.52 ± 0.14
2011-06-01 (MJD: 55713.0)	1.22 ± 0.09
2011-06-02 (MJD: 55714.0)	1.61 ± 0.09
2011-06-05 (MJD: 55717.0)	1.53 ± 0.09
2011-07-24 (MJD: 55766.0)	1.91 ± 0.28
2011-08-10 (MJD: 55783.0)	2.07 ± 0.09

by $\sim$10 min, for a total time baseline of $\sim$30 min in that sequence. Typically, two to four such sequences are obtained per field per lunation; the cycle is generally repeated the next lunation, marching through the RA range during the year. The time baselines now extend to 6 yr with up to $\sim$300 exposures per pointing over much of the area surveyed so far. This represents an unprecedented coverage in terms of the combined area, depth and number of epochs. The photometric flux data of 4C +49.22 are retrieved through the Catalina Surveys Data Release services[9] (see Fig. 6).

6 γ-RAY FLARE AND TIME VARIABILITY

To investigate the behaviour of this source, in particular the flaring state phase, we extracted the light curves from the entire data set using different time binnings (1 week, 3 d and 1 d time bins) with GTLIKE. The source spectrum was fitted with a power-law function. In the case of 1 d time bins, we fixed the photon index to the value found in the whole energy band, integrating over 3 yr of data. For longer time bins the photon index was left free to vary. The lowest panel of Fig. 6 shows the whole *Fermi*-LAT light curve with a weekly time bins. We report in the same figure radio and optical long-term observations by Metsähovi and *Planck* and CSS. Fig. 7 shows the parts of the multifrequency light curves during the main flaring activity, increasing in frequency from the top to the bottom panel. We studied the evolution of spectral shape during the flaring state for the X-ray and γ-ray components. We show in Fig. 7, the

photon index values versus time with overlaid *Fermi*-LAT light-curve shape in the inset panels. We performed a linear regression to evaluate the dependence between flux values and spectral indices, for *Fermi*-LAT no spectral evolution is evident during the flaring state with a regression coefficient of $r \sim 0.01$, but for the X-rays, a softer when brighter behaviour consistent with a shift in the synchrotron peak during the flaring state is noticeable ($r \sim 0.74$).

A direct comparison of the *Fermi*-LAT and CSS light curves clearly shows that an optical brightening occurred at the time of the γ-ray flare. Since no optical data for the same filter are available for the post-flare relaxing phase, we cannot estimate any time lag. Although the *Swift*-XRT data only cover a limited time range (see Fig. 7), these observations suggest a strong correlation between the X-ray and GeV flux. This correlation is illustrated in Fig. 8 where we have plotted the γ-ray versus X-ray flux at the times of the X-ray *Swift*-XRT measurements. During the period of the last *Swift*-XRT observation the source was not detected by *Fermi*-LAT and we did also include the UL in Fig. 8. The γ-ray flux for each point was obtained by linear interpolation of the 1-d bin LAT light curve. With only nine X-ray points available a standard discrete cross-correlation function (DCCF) would be very poorly sampled. On time-scales longer than the flare lengths of a few days the DCCF contains no significant information. It is however possible to use the DCCF on shorter time-scales to estimate a time lag between the X-ray and γ-ray variations. In Fig. 9, we show the DCCF for lags less than 3 d computed by oversampling the 1 d binned LAT light curve by a factor of 19, to give a larger oversampling, before correlating it with the X-ray points. The Gaussian fit, which is also shown in the figure, gives an estimated time lag $\Delta t = -0.4 \pm 1.0$ d (where negative lag means X-rays preceding γ-rays). Uncertainty estimates were made by two different Monte Carlo methods: the model independent approach by Peterson et al. (1998) and by simulated flare light curves. In the second approach double-sided exponential flares were sampled in a similar manner to the observations in order to investigate uncertainties due to the precise timing of the X-ray observations. The two methods gave consistent estimates.

We analysed the γ-ray flare of 2011 May 15 (MJD 55696), using the following function $F(t)$, already proposed in Abdo et al. (2010c), to fit the γ-ray light-curve shape during each single flare:

$$F(t) = F_c + F_0 \left(e^{\frac{t_0 - t}{T_r}} + e^{\frac{t - t_0}{T_d}} \right)^{-1}. \tag{5}$$

Here, F_c represents the baseline of the flux light curve, F_0 measures the amplitude of the flares, t_0 describes approximatively the time of the peak (it corresponds to the actual maximum only for symmetric flares), T_r and T_d the time of the rise and decay of each flare, respectively. Fig. 10 shows the light curve for the main flaring period that occurred in 2011 May, with the fit function superimposed. In Table 10, we reported the fit parameter value. Using this technique it is also possible to estimate the shortest time variability (to be conservative, the shortest value extracted is $\Delta t = 2T_r = 0.33$ d), which is used to put an important constraint on the radiative region size $R_{rad} \le (c\Delta t \mathcal{D})/(1 + z)$, where c is the speed of light, $\mathcal{D} = 1/(\Gamma(1 - \beta cos\theta))$ is the Doppler beaming factor, Γ the bulk Lorentz factor, θ the viewing angle and z the cosmological redshift. Using the Doppler factors obtained from the SED fitting procedure, which are in agreement with blazars with strong γ-ray emission (Savolainen et al. 2010), we can estimate that R_{rad} is $\lesssim 2.5 \times 10^{16}$ cm for $\mathcal{D} = 20$ and $\lesssim 3.8 \times 10^{16}$ cm for $\mathcal{D} = 30$.
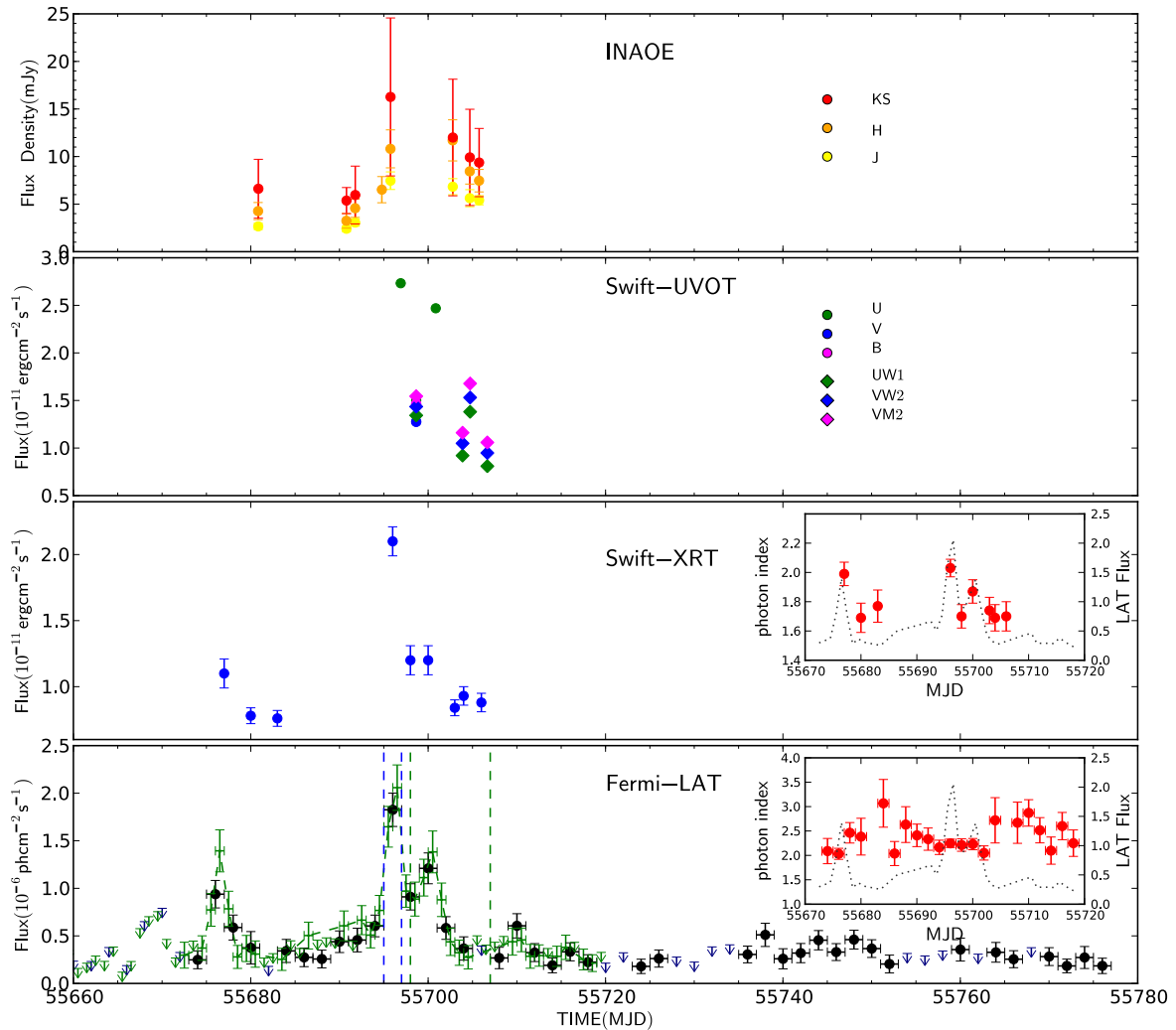
Figure 7. Multifrequency light curves zoomed in to the main flaring period (2011 May). In the first panel INAOE data points are shown in the different filters (described in Section 5.3); in the second panel, *Swift*-UVOT (described in Section 4); in the third panel, *Swift*-XRT (described in Section 4); and in the fourth panel, *Fermi*-LAT 1 d time bin data, are shown (described in Section 2). The blue and green dashed lines represent the two states considered in the SED modelling. The inset panels report the spectral indices coming from the power-law spectral fit in each bin with superimposed the *Fermi*-LAT γ-ray light curve.

7 RADIO-TO-γ-RAY SED

Variability is a powerful diagnostic for the physics of blazars but creates difficulties in the broad-band SED analysis because theoretical models can be effectively constrained only with sufficiently well time resolved multifrequency data. For example *Fermi*-driven observing campaigns are demonstrating the role of SSC emission for FSRQ objects (Böttcher, Reimer & Marscher 2009), while the ERC process is being used in fitting also the SEDs of BL Lac objects. First clues, suggesting a smooth transition between the division of blazars into BL Lac objects and FSRQs, are emerging in some studies (e.g. Cavaliere & D'Elia 2002; Giommi et al. 2012a; Sbarrato et al. 2012). Our *Fermi*, *Swift* and *Planck* results on the FSRQ 4C +49.22 are pointing out some features more typical of BL Lac objects, and therefore support this hypothesis.

The big blue-bump (thermal disc emission) in 4C +49.22 appears clearly in the low-emission state SED (see Figs 11 and 12), which is based on archival data; however, it is completely overwhelmed by the continuous synchrotron emission during the γ-ray flaring state. The lack of observable thermal disc emission is a common feature

in BL Lac objects, for which contribution from the accretion disc is negligible in both low and high activity states.

The SED of 4C +49.22 obtained during two epochs, flare and post-flare, through *Fermi*, *Swift*, *Planck* and radio–optical simultanous observations, appears consistent with a BL Lac object. Even a distinct bulk-Compton spectral excess generated by adiabatic expansion of the emitting region and a cold population of electrons, occasionally observed in some FSRQs, is not evident in the X-ray spectrum of this blazar. To evaluate the numerical model of the SED, we used the desktop version of the online code developed by AT (e.g. Massaro et al. 2006; Tramacere et al. 2009; Tramacere, Massaro & Taylor 2011) which finds the best-fitting parameters of the numerical modelling by a least-square χ^2 minimization.

In the following subsections, we report simultaneous MW SED modelling using both the two-zone SSC and the single zone SSC+ERC scenarios, since these different models both fit the simultaneous SED data of 4C +49.22.
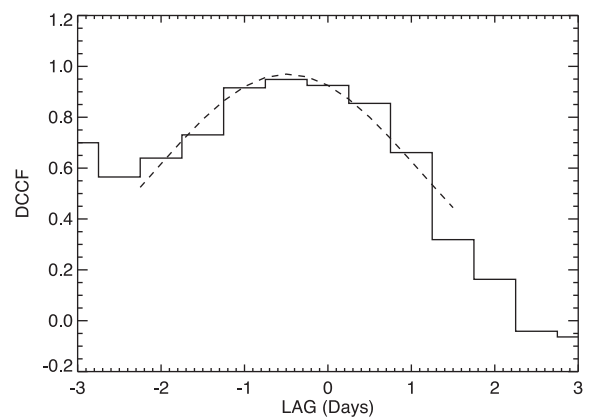
The numerical model self-consistently evaluates the energy content in the resulting equilibrium electron distribution, and compares

Table 9. Magnitudes and flux densities of 4C +49.22 with INAOE Telescope.

Filters	Date	Magnitude	Flux (mJy)
J	2011-04-29 (MJD: 55680.84)	14.45 ± 0.07	2.66 ± 0.32
	2011-05-09 (MJD: 55690.78)	14.55 ± 0.07	2.41 ± 0.29
	2011-05-10 (MJD: 55691.77)	14.29 ± 0.07	3.06 ± 0.37
	2011-05-14 (MJD: 55695.75)	13.33 ± 0.07	7.46 ± 0.92
	2011-05-21 (MJD: 55702.77)	13.42 ± 0.07	6.83 ± 0.84
	2011-05-23 (MJD: 55704.69)	13.63 ± 0.09	5.62 ± 0.89
	2011-05-24 (MJD: 55705.74)	13.68 ± 0.05	5.40 ± 0.47
H	2011-04-29 (MJD: 55680.82)	13.50 ± 0.08	4.26 ± 0.90
	2011-05-09 (MJD: 55690.78)	13.80 ± 0.09	3.24 ± 0.77
	2011-05-10 (MJD: 55691.76)	13.42 ± 0.08	4.56 ± 0.96
	2011-05-13 (MJD: 55694.77)	13.04 ± 0.08	6.51 ± 1.37
	2011-05-14 (MJD: 55695.75)	12.49 ± 0.07	10.8 ± 1.99
	2011-05-21 (MJD: 55702.76)	12.40 ± 0.07	11.7 ± 2.16
	2011-05-23 (MJD: 55704.69)	12.76 ± 0.06	8.44 ± 1.33
	2011-05-24 (MJD: 55705.74)	12.89 ± 0.06	7.46 ± 1.18
*K*s	2011-04-29 (MJD: 55680.85)	12.50 ± 0.11	6.61 ± 3.09
	2011-05-09 (MJD: 55690.79)	12.73 ± 0.06	5.37 ± 1.37
	2011-05-10 (MJD: 55691.78)	12.62 ± 0.12	5.95 ± 3.03
	2011-05-14 (MJD: 55695.75)	11.53 ± 0.12	16.2 ± 8.30
	2011-05-21 (MJD: 55702.78)	11.86 ± 0.12	12.0 ± 6.12
	2011-05-23 (MJD: 55704.69)	12.07 ± 0.12	9.91 ± 5.05
	2011-05-24 (MJD: 55705.74)	12.13 ± 0.09	9.36 ± 3.58

Figure 9. DCCF using the *Swift*-XRT data and the *Fermi*-LAT 1 d binned γ-ray light curve, The dashed curve is a Gaussian fit to the DCCF peak. The time lag is estimated to be -0.4 ± 1.0 d (negative means X-rays leading γ-rays).
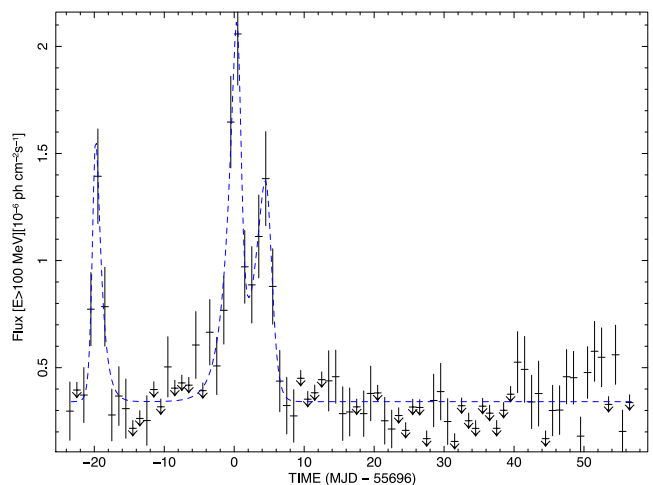
Figure 10. One day time bin light curve of *Fermi*-LAT data zoomed in to the flaring period of 2011 May with superimposed fitting function shown as a blue dashed line.

Figure 8. γ-ray versus X-ray flux at the times of *Swift*-XRT observations. *Fermi*-LAT fluxes were interpolated from the 1 d binned γ-ray light curve.

Table 10. Parameter values extracted from the flare shape fit.

t_{max} (MJD)	$T_r \pm$ err (d)	$T_d \pm$ err (d)
55676.2	0.33 ± 0.07	0.81 ± 0.15
55696.3	1.69 ± 0.24	0.29 ± 0.05
55700.4	1.96 ± 0.34	0.54 ± 0.11

this value to the magnetic-field energy density (Tramacere et al. 2011). The minimum energy content of the source is released near equipartition conditions between the magnetic field *B* power and radiating particle energy power in the jet (e.g. Dermer & Atoyan 2004; Dermer et al. 2014). Equipartition ratio values can be used to pick out a preferred scenario because the synchrotron spectrum implies minimum jet power. Our SED fit results for 4C +49.22 (Figs 11 and 12, Tables 11 and 12) suggest that the single zone, two processes (SSC plus ERC from both disc and torus) scenario is slightly preferred with respect to the two-zone and single process SSC model. In particular the two-zone SSC model fit points out that the energetics are very far from the equipartition condition for the fast emission blob responsible for the IC GeV γ-ray component.

7.1 Two zones, single SSC process

A single flaring emission zone with a leptonic SSC process is a model often used for high-energy peaked (and TeV) blazars. This scenario represents the first step in SED modelling attempts. One-zone models usually have difficulty reproducing highly variable states and composite X-ray spectra often observed in the SEDs of FSRQs and low/intermediate-energy peaked BL Lac objects. In this view a two-zone SSC model was applied to fit the SED of 4C +49.22, which allows us to take into account, in the fit attempt, the soft X-ray excess and the XRT spectral shape for the
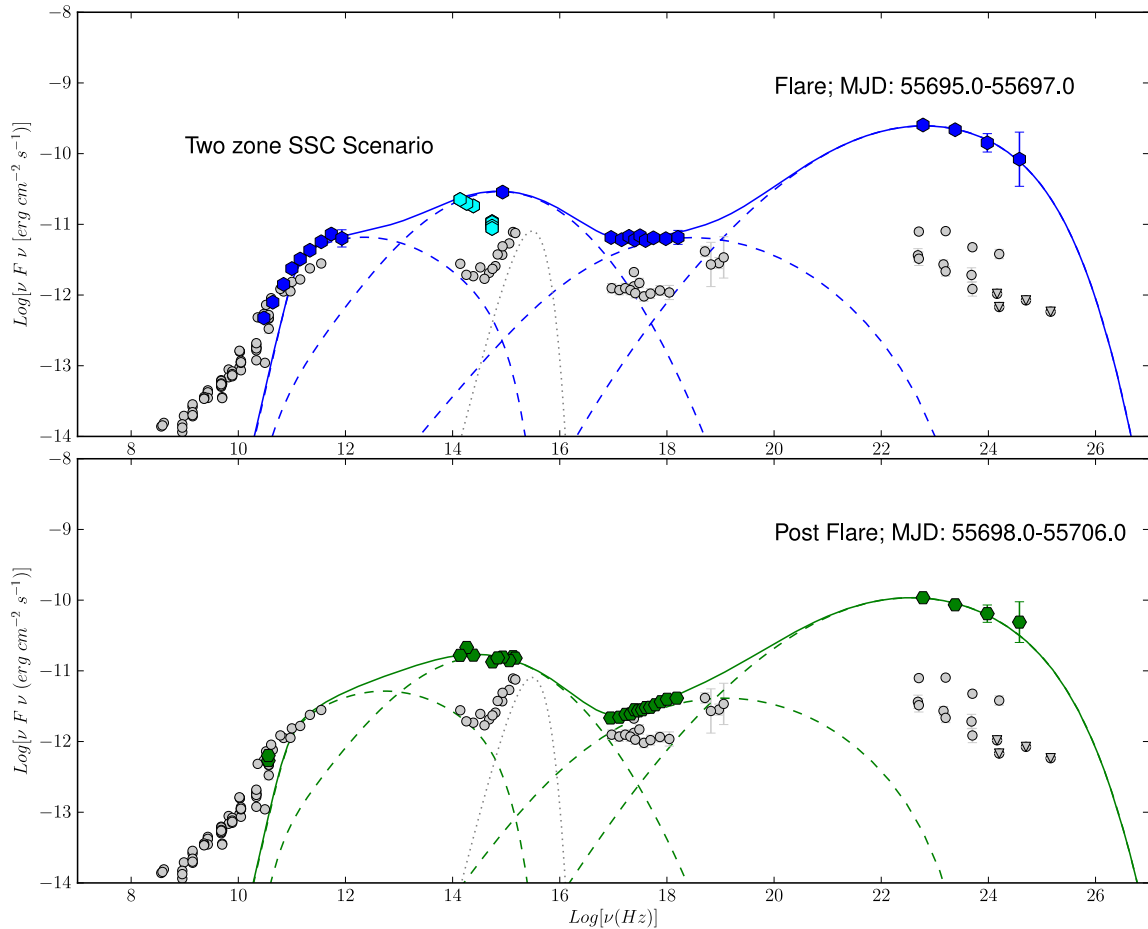
Figure 11. SED of 4C +49.22 at different epochs with fit models (solid lines) with a two-zone SSC code. The X- and γ-ray flare is evident. Simultaneous data during the flare of 2011 May 15 (MJD 55696) are shown in blue; the quasi-simultaneous data of CSS and INAOE are shown in cyan; post-flare (i.e. *Fermi*-LAT and *Swift*-XRT data are integrated from 2011 May 17 to 25, MJD 55698–55706) data are shown in green; archival or low state data are shown in grey. The grey dashed lines represent the different components, synchrotron and IC, used in the fitting procedure relative to each zone. The dotted line is the estimated contribution coming from the disc fitted to archival data.

flare state of 2011 May 15 (characterized by a photon index of 2.03 ± 0.06, Table 4), and allows us to connect in the fit the simultaneous XRT and LAT data. Double leptonic emission zones have been recently invoked to fit simultaneous blazar SED data (for example, Georganopoulos & Kazanas 2003; Liu & Shen 2007; Abdo et al. 2011; Moraitis & Mastichiadis 2011; Tavecchio et al. 2011), albeit at the expense of more free parameters.

The flare and post-flare epochs in the SED of 4C +49.22, based on simultaneous data and on archival data representative of the quiet state, are shown in Fig. 11 with the two-zone SSC models.

The hypothesis of two regions emitting through the SSC process is recently used in several cases of SED modelling. For example, a scenario based on a first SSC emission region encompassing the whole jet cross-section plus a second, compact and energetic SSC emission region defined by a high-bulk Lorentz factor blob responsible for the rapidly varying γ-ray emission is used in some SED models (Tavecchio et al. 2011; Ghisellini & Tavecchio 2008).

The two emitting blobs for 4C +49.22 are thought to represent a compact and faster emission region filled with fresh and high-energy electrons, and a larger, slower and diluted region accounting for the radio-band emission from older and lower energy cooling electrons, representing the surrounding plasma of the jet. The γ-ray emission blob is modelled with a bulk Doppler factor $\mathcal{D}_1 = 21.1$,

size $R_1 = 7.5 \times 10^{15}$ cm, intensity of the tangled magnetic field in the region of $B_1 = 0.25$ G. The instantaneous electron injection is self-consistently balanced with particle escape on a time-scale of the order of $t_{\rm esc} = R/c$.

The radio-band and hard X-ray emitting blob is reproduced using a much larger emitting region characterized by parameter values $\mathcal{D}_2 = 15$, $R_2 = 5.5 \times 10^{16}$ cm and $B_2 = 0.10$ G. Relativistic Doppler beaming factors of the two zones are found to be consistent with the range of values found in the maps made from 2008 up to 2012 of the MOJAVE programme (Lister et al. 2013). These two regions move relativistically along the jet, oriented at an angle at least $\theta < 38°$ with respect to the line of sight.

The kinetic partial differential equation of this model describes the evolution of the particle energy distribution after the injection of freshly accelerated electrons, with an instantaneous rate $Q(\gamma)$ equal to a power law turning into a log-parabola function in the high-energy tail (Landau et al. 1986; Massaro et al. 2006) whose functional form is

$$Q(\gamma) = \begin{cases} (\gamma/\gamma_0)^{-s} & \text{if } \gamma \leq \gamma_0 \\ (\gamma/\gamma_0)^{-(s+r\log(\gamma/\gamma_0))} & \text{if } \gamma > \gamma_0, \end{cases} \quad (6)$$
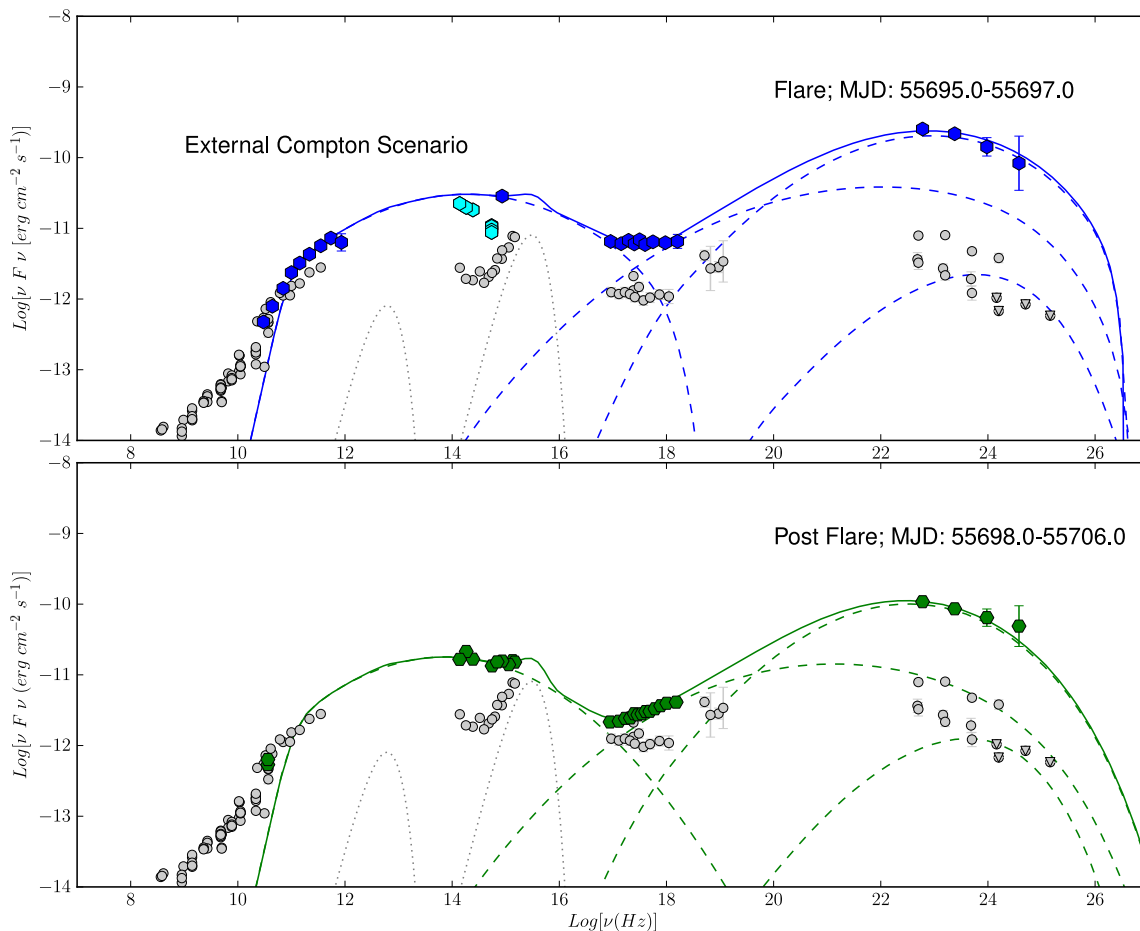
Figure 12. SED of 4C +49.22 at different epochs and relative fit models (solid lines) with a single zone and two-processes, SSC and ERC on disc and torus, code. Simultaneous data during the flare of May 15 are shown in blue; the quasi-simultaneous data of CSS and INAOE are shown in cyan; post-flare (i.e. *Fermi*-LAT and *Swift*-XRT data are integrated from May 17 to 25) data are shown in green; archival or low state data are shown in grey. The grey dashed lines represent the different components, synchrotron and IC, used in the fitting procedure. The dotted line is the estimated contribution coming from the disc fitted to archival data and the torus.

where γ_0 is the energy at the turnover frequency, s is the spectral index at the reference energy γ_0 and r is the spectral curvature. The respective values of parameters for both zones are reported in Table 11 for the flaring phase and Table 12 for the post-flare decreasing activity.

7.2 Single zone, SSC and ERC processes

The high-power MeV–GeV bolometric emission seen in flaring γ-ray FSRQs, can usually be better described by external-jet Comptonization of radiation (ERC) models. In this case, the seed photons for the IC process are typically UV photons generated by the accretion disc surrounding the black hole (BH), and reflected towards the jet by the BLR clouds within a typical distance from the accretion disc of the order of 1 pc (Sikora, Begelman & Rees 1994). Another component of external-jet seed photons in the IR band for the scattering is likely provided by a dust torus (DT; see e.g. Sikora, Begelman & Rees 1994). In this case, the cooling of relativistic electrons is dominated by Comptonization of near- and mid-IR radiation from ambient dust of the torus. This behaviour has already been found in FSRQs in the EGRET era (e.g. Sikora, Begelman & Rees 1994; Sokolov & Marscher 2005; Sikora, Moderski & Madejski 2008; Sikora et al. 2009). A model taking into account leptonic

SSC emission with the relevant addition of leptonic ERC from a single active blob (the single zone two-process model) can also be used to explain the two-epoch SEDs of 4C +49.22 as shown in Fig. 12. An accretion disc emission component is clearly seen in our archival data of the quiet activity state (bottom panel of Fig. 12) and this could be the origin of the dominant IC γ-ray radiation. In the SSC plus ERC hybrid model for 4C +49.22, X-ray emission can still be fitted as an SSC process, while the MeV–GeV γ-ray emission detected by *Fermi* can be fitted well by dominant ERC emission from the thermal disc, DT and BLR dissipation region. For this model fit, an equilibrium version of the time-dependent jet model reported in Tramacere et al. (2011) was used.

For the ERC emission, all the direct accretion disc radiation field, accretion disc emission reprocessed in the BLR and the radiation field from the DT illuminated by the disc are taken into account. We assumed the same electron energy distribution $Q(\gamma)$ with functional form equal to a power law turning into a log-parabola function in the high-energy tail described above, for the single active zone emitting via SSC and ERC processes. In this case, the single emitting blob is modelled with $\mathcal{D} = 20.1$, $R = 6.6 \times 10^{16}$ cm and $B = 0.10$ G. We estimated an accretion disc with physical characteristics using the UV data. We used the observations during the lowest phase of our data set to constrain the clear sign of thermal emission coming from the

Table 11. SED modelling parameters using a single zone SSC+ERC and a two-zones SSC for the flare period (blue/filled points in Figs 11 and 12). * indicates that the parameters are frozen to typical values. ** Value obtained describing the archival data.

Parameters	SSC(slow)+SSC(fast)	SSC+ERC
$\chi^2_{\rm red}$	0.29	0.44
$\log_{10}(R)$(cm)	$16.74^*/15.88 \pm 1.06$	16.82 ± 0.23
B (G)	$0.10^*/0.25 \pm 0.04$	0.10 ± 0.13
$\mathcal{D}$	$15^*/21.1 \pm 0.4$	20.1 ± 1.2
N(cm^{-3})	$2649.1 \pm 105.3/408.9 \pm 59.9$	176.9 ± 19.9
$\log_{10}(\gamma_{\min})$	$0.3^*/1.9 \pm 0.8$	1.19 ± 1.05
$\log_{10}(\gamma_{\max})$	$4^*/6^*$	5.50 ± 1.07
LogParab.+Power-law		
$\log_{10}(\gamma_0)$	$1.78^*/2.77 \pm 1.26$	1.83 ± 0.43
r	$0.8^*/1.11 \pm 0.54$	0.43 ± 0.05
s	$1.23 \pm 0.04/0.54 \pm 0.12$	1.32 ± 0.72
Disc ** − BLR − DT		
$L_{\rm disc}$ (erg s^{-1})	–	4×10^{45}
$T^{\max}_{\rm disc}$ (K)	–	5×10^4
$r^{\min}_{\rm BLR}$ (cm)	–	1×10^{18}
$r^{\max}_{\rm BLR}$ (cm)	–	2×10^{18}
$\tau_{\rm BLR}$	–	0.1
$r_{\rm DT}$ (cm)	–	1×10^{19}
$\tau_{\rm DT}$	–	0.1

Table 12. SED modelling parameters using a single zone SSC+ERC and a two-zones SSC for the post-flare period (green/filled points in Figs 11 and 12). * indicates that the parameters are frozen to a typical values. ** Value obtained describing the archival data.

Parameters	SSC(slow)+SSC(fast)	SSC+ERC
$\chi^2_{\rm red}$	0.23	0.20
$\log_{10}(R)$(cm)	$16.74^*/15.92 \pm 0.76$	16.63 ± 0.77
B (G)	$0.1^*/0.07 \pm 0.02$	0.12 ± 0.09
$\mathcal{D}$	$15^*/33.3 \pm 1.9$	22.9 ± 5.4
N(cm^{-3})	$640.6 \pm 22.9/434 \pm 15.3$	275.2 ± 16.1
$\log_{10}(\gamma_{\min})$	$0.3^*/0.0009 \pm 0.0001$	1.74
$\log_{10}(\gamma_{\max})$	$4.0^*/6.0^*$	10.4 ± 5.3
LogParab.+Power-law		
$\log_{10}(\gamma_0)$	$1.77^*/2.77 \pm 0.51$	1.66 ± 0.31
r	$0.8^*/1.04 \pm 0.27$	0.52 ± 0.17
s	$0.9 \pm 0.1/0.7 \pm 0.2$	1.06 ± 0.15
Disc ** − BLR − DT		
$L_{\rm disc}$ (erg s^{-1})	–	4×10^{45}
$T^{\max}_{\rm disc}$ (K)	–	5×10^4
$r^{\min}_{\rm BLR}$ (cm)	–	1×10^{18}
$r^{\max}_{\rm BLR}$ (cm)	–	2×10^{18}
$\tau_{\rm BLR}$	–	0.1
$r_{\rm DT}$ (cm)	–	1×10^{19}
$\tau_{\rm DT}$	–	0.1

accretion disc and set a reference value of $L_{\rm disc} \simeq 4 \times 10^{45}$ erg s^{-1}. The temperature profile of a standard disc emitting locally as a blackbody following Ghisellini & Tavecchio (2009) is

$$T^4_{\rm disc}(R) = \frac{3R_{\rm S} L_{\rm disc}}{16\pi\epsilon\sigma_{\rm SB} R^3} \left(1 - \sqrt{\frac{3R_{\rm s}}{R}}\right), \tag{7}$$

where $\sigma_{\rm SB}$ is the Stefan–Boltzmann constant and $R_{\rm S} = 2GM_{\rm BH}/c^2$ is the Schwarzschild radius. We assumed that the accretion disc ex-

tends from $R_{\rm in} \simeq 3R_{\rm S}$ to $R_{\rm out} \simeq 500R_{\rm s}$. Since $T_{\rm disc}(R)$ peaks at $R \simeq 4R_{\rm S}$, we used the UV observations of the accretion disc to constrain the $T_{\rm disc}$ and use equation (7) to calculate $R_{\rm S}$. Using our set of data, we extracted a value of $T_{\rm disc} \simeq 5 \times 10^4$ K. Assuming an accretion efficiency $\epsilon \simeq 0.1$, we obtain a $R_{\rm S} \simeq 1.2 \times 10^{14}$ cm. The value of BH mass $M_{\rm BH}$ coming from the $R_{\rm S}$ evaluation is about 4.0×10^8 M$_\odot$. This value of $M_{\rm BH}$ we found using the UV observations of the accretion disc is compatible, assuming an accretion rate of 0.74 M$_\odot$ yr^{-1} (coming from the formula that links the luminosity to the accretion mass rate $L_{\rm disc} = \eta \dot{M} c^2$ erg s^{-1}) with the one obtained by Shields et al. (2003) using the virial assumption with the evaluation of FWHM of the broad Hβ line. However, it is less than the mass of the BH extracted by Decarli et al. (2008) using the estimation of the luminosity of the host galaxy. The BLR is represented as a spherical shell of reprocessing material with radial Thomson depth $\tau_{\rm BLR} = 0.1$. If $L_{\rm disc} = \eta \dot{M} c^2$ erg s^{-1} is the total luminosity of the disc (where η is the accretion efficiency) the BLR is assumed to be a shell located at a distance from the central BH of $r_{\rm BLR} = 10^{17}\sqrt{L_{\rm disc}/10^{45}}$ cm (Ghisellini & Tavecchio 2008). The energy dissipation, if it is assumed to be producing the γ-ray flux, must occur at hundreds of Schwarzschild radii from the BH, in order to avoid $\gamma\gamma$ pair production absorption. Similarly the DT is placed at distance from the central BH of $r_{\rm DT} = 1 \times 10^{19}$ cm. In our model, we fixed values for the distance where the energy dissipation occurs within the BLR region, $r^{\min}_{\rm BLR} = 1 \times 10^{18}$ cm and $r^{\max}_{\rm BLR} = 2 \times 10^{18}$ cm during the first flare 2011 May 15 and the post-flare phase of 2011 May 17–25. This implies an emission region placed at about 0.32–0.65 pc from the central BH, in agreement with previous ERC scenarios for FSRQs (Dermer et al. 2009; Ghisellini & Tavecchio 2009).

Both the two-zone SSC and single zone SSC+ERC models fits appear appropriate to represent the observed high-state and post-flare SED of 4C +49.22 built for the first time with simultaneous data from the three space missions *Fermi*, *Swift* and *Planck*. Equipartition ratio values, numbers of emission components, number of needed model fit parameters, their physical values, the agreements with previous models and VLBA data can alternatively support both scenarios. The manifest thermal blue-bump is completely overwhelmed by the non-thermal synchrotron emission during the flare, evidence which favours the double-zone SSC picture. Taking into account the multi-epoch VLBA results presented in Section 5.1 can exclude flaring GeV emission produced by jet knots placed at large distance, of the order of tens of parsecs (Lister et al. 2013), from the radio core and the BLR region. This can support a more canonical SSC+ERC model for FSRQ sources over the two-zone SSC, because active regions, if located at sub-parsec distances, would lie in proximity of the BLR photon field and if located within a few parsecs would lie at the scale of the molecular DT IR photon environment available for Comptonization.

8 DISCUSSION AND CONCLUSIONS

We have presented simultaneous *Fermi*, *Swift* and *Planck*, optical and near-IR flux observations and radio-band flux-structure observations of the blazar 4C +49.22 (S4 1150+49, OM 484, SBS 1150+497, $z = 0.334$). This is one of few cases where time-simultaneous data from three such space missions are available, in particular during a bright GeV flare.

The GeV outburst of this FSRQ was observed by the LAT around 2011 May 15 after a prolonged period of low γ-ray activity. The γ-ray flare was observed simultaneously in X-ray data, with no measurable time lag (Fig. 9). 4C +49.22 showed synchrotron emission

peaked in the near-IR and optical wavebands with X-ray spectral softening and time-correlated variability in microwave/X-ray/GeV energy bands as observed more commonly in BL Lac objects rather than FSRQs. As seen in Section 7 the single SSC mechanism, adopted usually for BL Lac objects, can also explain the radio-to-γ-ray SED of this FSRQ during the flaring state and following epoch (Figs 11 and 12).

This is also one of the first cases where a two-zone SSC model (slow+fast in-jet components) and a single-zone SSC+ERC model (BLR and DT components) both appear appropriate to represent the high γ-ray state multifrequency SED of a FSRQ. Opposite to the majority of the 'strawman' models overimposed to SED data, our claim follows a true SED modelling through the best-fitting model calculations with minimization over the physical parameter grid (Tramacere et al. 2011).

We briefly recall the several aspects that make 4C +49.22 a particularly interesting object for high-energy studies. 4C +49.22 is a powerful and core-dominated FSRQ showing a bright and structured kiloparsec X-ray jet, diffuse thermal soft X-ray emission produced by the host galaxy and/or galaxy group medium, and a significant fluorescent Kα emission line (equivalent width $\simeq$ 70 eV) from cold iron (Gambill et al. 2003; Sambruna et al. 2006b). The Fe line detection indicates that even in the X-ray band the beamed jet emission in the low activity states does not completely swamp the accretion-related emission, qualifying this source as a good candidate to investigate the disc–jet connection with multifrequency observations (Grandi & Palumbo 2004). This object is also a high-luminosity FSRQ characterized by a one-sided core–jet radio structure, where the strong and compact jet extends 6 mas (i.e. about 28 pc) in the south-west direction. The 5 GHz VLBI polarization structure of the source is relatively simple (Qi, Zhang & Nan 2009), where fractional polarization ($\sim$1 per cent) is basically concentrated in the core region, and the direction of the mas-scale magnetic field is consistent with jet direction. *Chandra* resolved and identified in a hotspot of 4C +49.22 and compact X-ray substructures (Tavecchio et al. 2005). Finally, simultaneous disc and BLR luminosities show $L_{BLR}/L_{disc} = 0.08$ (Sambruna et al. 2006b) and the estimated mass of the SMBH of 4C +49.22 is $4.0 \times 10^8\,M_\odot$ consistent with what was found by Shields et al. (2003) and Decarli et al. (2008). Our results can be summarized as follows.

8.1 A class-transitional FSRQ?

4C +49.22 is an FSRQs showing a shift of two orders of magnitude in the frequency of the synchrotron peak (from $\sim 10^{12}$ to $\sim 10^{14}$ Hz) during the GeV γ-ray flare. This was accompanied by a contemporaneous marked spectral change in the X-ray energy band. In particular, Giommi et al. (2012b) have shown that the distribution of synchrotron emission peaks of FSRQs are centred on a frequency of 10^{13} Hz, and the change seen in 4C +49.22 can be interpreted as phenomenological transition from an FSRQ to a BL Lac object, with the thermal blue-bump overwhelmed by synchrotron jet emission during the flaring state. This phenomenology can be taken into account in blazar classification and demography paradigms (Giommi et al. 2012a; Giommi, Padovani & Polenta 2013) even if occurring in short, transitory, phases of the blazar's life, and can be in agreement with some recent hypotheses suggesting a smooth transition between the division of blazars into BL Lac objects and FSRQs (e.g. Cavaliere & D'Elia 2002; Giommi et al. 2012a; Sbarrato et al. 2012). An example of a similar SED peak shift for flaring states is represented by the well-known FSRQ PKS 1510−089 (Abdo et al. 2010b; D'Ammando et al. 2011).

The marked spectral softening of the X-ray spectrum, providing an unusual flat X-ray SED, is also a feature observed in intermediate synchrotron energy peaked BL Lac objects rather than FSRQs. In addition this soft X-ray spectrum does not show any distinct sign of a bulk-Compton origin, generated by the adiabatic expansion of the emitting region and a cold population of electrons, a feature found usually in FSRQs but missing in this case. SED data therefore suggest a contribution to the X-ray emission from different emission components, i.e. both synchrotron and IC (SSC and/or ERC) mechanisms, as usually observed for intermediate energy peaked BL Lac objects (for example Tagliaferri et al. 2000; Ciprini et al. 2004; Abdo et al. 2011).

Another interesting feature related to this is the optical spectrum. SSDS DR7 and DR8 optical spectra (Adelman-McCarthy et al. 2008), obtained during low emission states, show a rest frame equivalent width (EW) of the broad Hα emission line of about 300 Å. We fitted the synchrotron bump of the SED during the γ-ray flare epoch using a third degree polynomial function and we extrapolated using the best-fitting model the value of the continuum at the Hα frequency. Provided that flux enhancement is due to non-thermal radiation only, the extrapolated continuum of 4C +49.22 at the frequency of the Hα emission line shows an increase of a factor of $\sim$23 during the γ-ray flaring state, resulting in a reduction of the emission line EW to about 13 Å, therefore approaching the limit considered for the BL Lac object class (blazars with rest-frame emission line EWs smaller than 5 Å). The usual classification of blazar subclasses using the rest frame EW definition can be misleading. Objects so far classified as BL Lac objects are turning out to be two physically different classes: intrinsically weak lined objects, more common in X-ray selected samples, and heavily jet-diluted broad lined sources, more frequent in radio selected samples (Giommi et al. 2012a, 2013).

8.2 Two-zone SSC versus single zone SSC+ERC models

The multifrequency SEDs (Figs 11 and 12) show the synchrotron emission outshining the thermal blue-bump emission that appeared evident in the low activity state. We modelled the radio-to-γ-ray SEDs for the flare state and the post-flare epoch. A single flaring blob with two different emission mechanisms (SSC and ERC) and a two-zone model with a single SSC process were applied to our SED data. The averaged low state built with archival data (grey points and blue-bump signature in Figs 11 and 12) can be described by including both the jet and disc contributions while the single zone SSC model fails. The disc emission is parametrized in terms of a blackbody from optical to soft X-rays, and the ERC modelling required also a torus emission component contributing to the IC scattering. Our two-zone SSC and single zone SSC+ERC model fits appears both appropriate to represent the observed high-state and post-flare SED of 4C +49.22, depending on the considered feature (equipartition ratio values, number of parameters, their values, agreements of parameters with previous model values estimated in literature, and agreement with VLBA parameter values and structure). The SSC+ERC is suggested to be slightly more preferred based on equipartition ratio, but the two-zone pure-SSC is still a valid alternative. The manifest thermal blue-bump is completely outshone by the non-thermal synchrotron emission during the flare, evidence which goes in the direction of the pure SSC scenario, which usually better represents the SEDs of BL Lac objects.

On the other hand, the multi-epoch VLBA results presented in Section 5.1 can exclude flaring GeV emission produced by jet knots placed at large distances, of the order of tens of parsecs (Lister

et al. [2013]), from the radio core and the BLR region. This suggests a non-negligible contribution of seed photons produced in the BLR for the IC up-scatter, strengthening the case for the hybrid SSC+ERC scenario. In general equipartition can be strongly violated during large γ-ray flare events. Previous SSC models applied to the SED of 4C +49.22 and fits of radio-to-X-ray emission of *Chandra*-resolved subcomponents seen in the terminal part of the jet (Tavecchio et al. [2005]) support this violation. This suggests IC scattering of synchrotron radiation by some special electron distribution with an excess of high-energy electrons, or CMB photons, or back-scattered central radiation. *Fermi*-LAT detected non-spatially resolved GeV emission from 4C +49.22 and which may have been an integrated combination of emission from different regions. In this view, the γ-ray flaring state (blue points in Figs [11] and [12]) likely can be better represented by the double zone SSC scenario.

8.3 Pair production opacity and relativistic beaming

The γ-ray flux of 4C +49.22 is variable with short time-scales (< 1 d). The rapid variability and the large γ-ray luminosity imply appreciable pair production opacity. The unbeamed source size estimated from the observed variability time-scale indicates that the source is opaque to the photon–photon pair production process if γ-ray and X-ray photons are produced cospatially. This assumption, however, firmly rests on the simultaneity of the flaring event as observed by *Fermi*-LAT and *Swift*-XRT. Simultaneous X-ray and γ-ray flare events have been measured in the past for other sources like 3C 454.3 (Abdo et al. [2009b]). Relativistic beamed jet and emission blobs can solve this problem. Following the arguments given in Mattox et al. ([1993]) and adopting the doubling flux time-scale of $t_d \sim 0.6$ d and the observed X-ray flux of $S_X = (2.1 \pm 0.1) \times 10^{-11} \mathrm{erg\,cm^{-2}\,s^{-1}}$ (as measured during the main flare in γ rays) at the observed photon frequency $\nu_X \simeq 10^{18}$ Hz (corresponding to the photons that interact with the GeV γ rays in the jet rest frame), we can estimate the Doppler factor $\mathcal{D}$ required for the photon–photon annihilation optical depth to be $\tau_{\gamma\gamma} < 1$. With the derived relation

$$\tau_{\gamma\gamma} \simeq \frac{\sigma_T d_L^2 S_X}{3 t_d c^2 E_X \mathcal{D}^4}, \tag{8}$$

where we assume the emission region linear size $R = c t_d \mathcal{D}/(1 + z) \simeq 2 \times 10^{16}$ cm and the source-frame photon energy $E_X = (1 + z) h \nu_x / \mathcal{D}$. Assuming the standard cosmology values we obtain $\mathcal{D} \gtrsim 8.3$. Omitting the requirement of cospatiality of the X-ray and γ-ray emission regions relaxes this limit. This can be compared with the estimate obtained from the VLBA superluminal motion, $\mathcal{D} > 4.3$. As long as the velocity of the VLBA jet is the same as the velocity of the outflow within the blazar emission zone, this implies that the photon–photon annihilation effects involving the X-ray emission generated within the jet are negligible.

8.4 Energy dissipation region

The location of the γ-ray emitting region is debated, although large distances from the BH are recently being favoured for about 2/3 of GeV FSRQs (e.g. Marscher et al. [2010]). 10 epochs of VLBA observations at 15 GHz (MOJAVE programme) of 4C +49.22 obtained from 2008 May to 2013 February point to Lorentz factor limits that are consistent with our SED modelling and to increasing flux density and polarization degree in the radio core after the GeV γ-ray flare. In addition, *Planck* simultaneous observations reveal spectral changes in the sub-mm regime associated with the γ-ray flare. Our

SED modelling is in agreement with multi-epoch VLBA results and takes into account this evolution observed between the flare on May 15 (blue SED data and Table [11]) and the post-flare (May 17–25) epoch (green SED data and Table [12]). The resulting compact emission region of 4C +49.22 suggests that nuclear optical/UV seed target photons of the BLR dominate the production of IC emission (Tavecchio et al. [2010]). Alternatively, if the volume involved in the γ-ray emission is assumed much smaller than jet length scales, like turbulent plasma cells flowing across standing shocks (Marscher [2014]), hour/day-scale variability can also be produced at several parsecs from the central engine. The VLBA flux density and polarization degree in the radio core both increased with the ejection of a new component close in time to the γ-ray flare epoch. The jet kinetic power and disc luminosity of 4C +49.22 follow the same trend observed for other powerful γ-ray FSRQs, where a large fraction of the accretion power is converted into bulk kinetic energy of the jet, and our SED models suggest a larger BLR size compared to previous estimates (Sambruna et al. [2006b]; Decarli et al. [2008]).

The detailed results about 4C +49.22 presented in this work followed the availability of simultaneous *Fermi*, *Swift*, *Planck* and VLBA observations triggered by the LAT-detected GeV outburst and by our *Swift* ToO follow-up programme. Such data allowed us to investigate multifrequency flux versus radio-structure relationships, build and constrain pure-SSC versus SSC+ERC SED physical model fits, study emission region localisation, energetics and the evolution of the multifrequency and high-energy SED during two different emission states for the source, and finally to extrapolate phenomenological features alternatively supporting the FSRQ or BL Lac nature of the source. 4C +49.22 is a powerful FSRQ, with a Fanaroff–Riley type II morphology and possesses a powerful radio/X-ray jet, but it can have its broad emission lines heavily diluted by a swamping non-thermal continuum during high-energy events. The synchrotron peak energy and the unresolved X-ray spectra resemble those of intermediate BL Lac objects. Simultaneous multifrequency data at low and high energies, from space-borne missions like *Fermi*, *Swift* and *Planck* are also needed in the future to correctly draw conclusions about the underlying physics, demography and cosmological evolution of γ-ray loud AGN.

---

[10] http://www.isdc.unige.ch/sedtool/
[11] http://tools.asdc.asi.it/SED/

REFERENCES

Abdo A. A. et al., 2009a, Astropart. Phys., 32, 193
Abdo A. A. et al., 2009b, ApJ, 699, 817
Abdo A. A. et al., 2010a, ApJS, 188, 405
Abdo A. A. et al., 2010b, ApJ, 721, 1425
Abdo A. A. et al., 2010c, ApJ, 722, 520
Abdo A. A. et al., 2011, ApJ, 730, 101
Ackermann M. et al., 2012, ApJS, 203, 4
Ade P. A. R. et al., 2013, preprint (arXiv:1303.5076)
Adelman-McCarthy J. K. et al., 2008, ApJS, 175, 297
Akujor C. E., Garrington S. T., 1991, MNRAS, 250, 644
Atwood W. B. et al., 2009, ApJ, 697, 1071
Barthelmy S. D. et al., 2005, Space Sci. Rev., 120, 143
Böttcher M., Reimer A., Marscher A. P., 2009, ApJ, 703, 1168
Burbidge E. M., 1968, ApJ, 154, L109
Burrows D. N. et al., 2005, Space Sci. Rev., 120, 165
Cavaliere A., D'Elia V., 2002, ApJ, 571, 226
Ciprini S., Tosti G., Teräsranta H., Aller H. D., 2004, MNRAS, 348, 1379
Cohen A. S., Lane W. M., Cotton W. D., Kassim N. E., Lazio T. J. W., Perley R. A., Condon J. J., Erickson W. C., 2007, AJ, 134, 1245
Condon J. J., Cotton W. D., Greisen E. W., Yin Q. F., Perley R. A., Taylor G. B., Broderick J. J., 1998, AJ, 115, 1693
Cusumano G. et al., 2010a, A&A, 510, A48
Cusumano G. et al., 2010b, A&A, 524, A64
DAmmando F. et al., 2011, A&A, 529, A145
Decarli R., Labita M., Treves A., Falomo R., 2008, MNRAS, 387, 1237
Dermer C. D., Atoyan A., 2004, ApJ, 611, L9
Dermer C. D., Finke J. D., Krug H., Böttcher M., 2009, ApJ, 692, 32
Dermer C. D., Cerruti M., Lott B., Boisson C., Zech A., 2014, ApJ, 782, 82
Dixon R. S., 1970, ApJS, 20, 1
Fanti C., Pozzi F., Dallacasa D., Fanti R., Gregorini L., Stanghellini C., Vigotti M., 2001, A&A, 369, 380
Fitzpatrick N., 1999, PASP, 111, 63
Gambill J. K., Sambruna R. M., Chartas G., Cheung C. C., Maraschi L., Tavecchio F., Urry C. M., Pesce J. E., 2003, A&A, 401, 505
Gehrels N. et al., 2004, ApJ, 611, 1005
Georganopoulos M., Kazanas D., 2003, ApJ, 594, L27
Ghisellini G., Tavecchio F., 2008, MNRAS, 386, L28
Ghisellini G., Tavecchio F., 2009, MNRAS, 397, 985
Giommi P., Padovani P., Polenta G., Turriziani S., D'Elia V., Piranomonte S., 2012a, MNRAS, 420, 2899
Giommi P. et al., 2012b, A&A, 541, A160
Giommi P., Padovani P., Polenta G., 2013, MNRAS, 431, 1914
González-Nuevo J., Argüeso F., López-Caniego M., Toffolatti L., Sanz J. L., Vielva P., Herranz D., 2006, MNRAS, 369, 1603
Grandi P., Palumbo G. G. C., 2004, Science, 306, 998
Gregory P. C., Scott W. K., Douglas K., Condon J. J., 1996, ApJS, 103, 427
Hardcastle M. J., 2006, MNRAS, 366, 1465
Hartman R. C. et al., 1999, ApJS, 123, 79
Hays E., Dona D., 2011, Astron. Telegram, 3313, 1
Hunt L. K., Mannucci F., Testi L., Migliorini S., Stanga R. M., Baffa C., Lisi F., Vanzi L., 1998, AJ, 115, 2594
Kalberla P. M. W., Burton W. B., Hartmann D., Arnal E. M., Bajaja E., Morras R., Pöppel W. G. L., 2005, A&A, 440, 775
Kuehr H., Witzel A., Pauliny-Toth I. I. K., Nauber U., 1981, A&AS, 45, 367
Landau R. et al., 1986, ApJ, 308, 78
Leahy J. P. et al., 2010, A&A, 520, A8
León-Tavares J., Valtaoja E., Giommi P., Polenta G., Tornikoski M., Lähteenmki A., Gasparrini D., Cutini S., 2012, ApJ, 754, 23
Lister M. L. et al., 2009, AJ, 137, 3718
Lister M. L. et al., 2013, AJ, 146, 120
Liu W.-P., Shen Z.-Q., 2007, ApJL, 668, L23
López-Caniego M., Herranz D., González-Nuevo J., Sanz J. L., Barreiro R. B., Vielva P., Argüeso F., Toffolatti L., 2006, MNRAS, 370, 2047
López-Caniego M., González-Nuevo J., Herranz D., Massardi M., Sanz J. L., De Zotti G., Toffolatti L., Argüeso F., 2007, ApJS, 170, 108
Lynds R., Wills D., 1968, ApJ, 153, L23
Mandolesi N. et al., 2010, A&A, 520, A3
Marscher A. P., 2006, in Philip A. H., Bregman J. N., eds, AIP Conf. Proc. Vol. 856, Relativistic Jets: The Common Physics of AGN, Microquasars, and Gamma-Ray Bursts. Am. Inst. Phys., New York, p.1
Marscher A. P., 2014, ApJ, 780, 87
Marscher A. P. et al., 2010, ApJ, 710, L126
,Massardi M., Burigana C., 2010, New Astron., Rev., 15, 678
Massardi M., López-Caniego M., González-Nuevo J., Herranz D., de Zotti G., Sanz J. L., 2009, MNRAS, 392, 733
Massaro E., Tramacere A., Perri M., Giommi P., Tosti G., 2006, A&A, 448, 861
Mattox J. R. et al., 1993, ApJ, 410, 609
Mattox J. R. et al., 1996, ApJ, 461, 396
Mennella et al., 2011, A&A, 536, A3
Moore R. L., Stockman H. S., 1981, ApJ, 243, 60

Moraitis K., Mastichiadis A., 2011, A&A, 525, A40

Nolan P. L. et al., 2012, ApJS, 199, 31

Orienti M., Venturi T., Dallacasa D., D'Ammando F., Giroletti G., Giovannini G., Vercellone S., Tavani M., 2011, MNRAS, 417, 359

Owen F. N., Puschell J. J., 1984, AJ, 89, 932

Peterson B. M., Wanders I., Horne K., Collier S., Alexander T., Kaspi S., Maoz D., 1998, PASP, 110, 660

Pittori C. et al., 2009, A&A, 506, 1563

Planck Collaboration I, 2011, A&A, 536, A1

Planck Collaboration II, 2011, A&A, 536, A2

Planck Collaboration VII, 2011, A&A, 536, A7

Planck Collaboration I, 2014, A&A, in press

Planck Collaboration VI, 2014, A&A, in press

Planck Collaboration XVI, 2014, A&A, in press

Planck Collaboration XXVIII, 2014, A&A, in press

Planck HFI Core Team 2011a, A&A, 536, A4

Planck HFI Core Team, 2011b, A&A, 536, A6

Poole T. S. et al., 2008, MNRAS, 383, 627

Pushkarev A. B., Kovalev Y. Y., Lister M. L., Savolainen T., 2009, A&A, 507, L33

Qi J.-W., Zhang H.-Y., Nan R.-D., 2009, Chin. Astron. Astrophys., 33, 251

Reyes L., D'Ammando F., Hoversten E., 2011, Astron. Telegram, 3353, 1

Roming P. W. A. et al., 2005a, Space Sci. Rev., 120, 95

Roming P. W. A. et al., 2005b, Space Sci. Rev., 120, 143

Rosset C. et al., 2010, A&A, 520, A13

Sambruna R. M., Gambill J. K., Maraschi L., Tavecchio F., Cerutti R., Cheung C. C., Urry C. M., Chartas G., 2004, ApJ, 608, 698

Sambruna R. M., Gliozzi M., Donato D., Maraschi L., Tavecchio F., Cheung C. C., Urry C. M., Wardle J. F. C., 2006a, ApJ, 641, 717

Sambruna R. M., Gliozzi M., Tavecchio F., Maraschi L., Foschini L., 2006b, ApJ, 652, 146

Savolainen T., Homan D. C., Hovatta T., Kadler M., Kovalev Y. Y., Lister M. L., Ros E., Zensus J. A., 2010, A&A, 512, A24

Sbarrato T., Ghisellini G., Maraschi L., Colpi M., 2012, MNRAS, 421, 1764

Schlegel D. J., Finkbeiner D. P., Davis M., 1998, ApJS, 500, 525

Shields G. A. et al., 2003, ApJ, 583, 124

Sikora M., Begelman M. C., Rees M. J., 1994, ApJ, 421, 153

Sikora M., Moderski R., Madejski G. M., 2008, ApJ, 675, 71

Sikora M., Stawarz Ł., Moderski R., Nalewajko K., Madejski G. M., 2009, ApJ, 704, 38

Sokolov A., Marscher A. P., 2005, ApJ, 629, 52

Stepanian J. A., Green R. F., Foltz C. B., Chaffee F., Chavushyan V. H., Lipovetsky V. A., Erastova L. K., 2001, AJ, 122, 3361

Tagliaferri G. et al., 2000, A&A, 354, 431

Tauber J. A. et al., 2010, A&A, 520, A1

Tavecchio F., Cerutti R., Maraschi L., Sambruna R. M., Gambill J. K., Cheung C. C., Urry C. M., 2005, ApJ, 630, 721

Tavecchio F., Ghisellini G., Bonnoli G., Ghirlanda G., 2010, MNRAS, 405, L94

Tavecchio F., Becerra-Gonzalez J., Ghisellini G., Stamerra A., Bonnoli G., Foschini L., Maraschi L., 2011, A&A, 534, A86

Teräsranta H. et al., 1998, A&AS, 132, 305

Tramacere A., Giommi P., Perri M., Verrecchia F., Tosti G., 2009, A&A, 501, 879

Tramacere A., Massaro E., Taylor A. M., 2011, ApJ, 739, 66

Voges W. et al., 1999, A&A, 349, 389

White N. E., Giommi P., Angelini L., 1994, IAU Circ., 6100, 1

White R. L., Becker R. H., Helfand D. J., Gregg M. D., 1997, ApJ, 475, 479

Wright E. L. et al., 2009, ApJS, 180, 283

Zacchei A. et al., 2011, A&A, 536, A5

[1]*ASI Science Data Center, Via del Politecnico snc, I-00133 Rome, Italy*

[2]*INAF Osservatorio Astronomico di Roma, Monte Porzio Catone,Via Frascati 33, I-00040 Rome, Italy*

[3]*INAF Istituto di Radioastronomia, I-40129 Bologna, Italy*

[4]*Dipartimento di Astronomia, Universita' di Bologna, via Ranzani 1, I-40127 Bologna, Italy*

[5]*ISDC Data Centre for Astrophysics, University of Geneva, Chemin d'Ecogia 16, Versoix, CH-1290, Switzerland*

[6]*Dipartimento di Fisica, Universitá degli Studi di Perugia, Via A. Pascoli, I-06123 Perugia, Italy*

[7]*INFN Sezione Perugia, Via A. Pascoli, I-06123 Perugia, Italy*

[8]*Instituto Nacional de Astrofisica, Optica y Electronica, Tonantzintla, Puebla, C.P 72860, Mexico*

[9]*Instituto de Física de Cantabria (CSIC-Universidad de Cantabria), Avda. de los Castros s/n, E-39005 Santander, Spain*

[10]*SISSA, Astrophysics Sector, via Bonomea 265, I-34136 Trieste, Italy*

[11]*Istituto di Astrofisica Spaziale e Fisica Cosmica-Bologna, INAF, via Gobetti 101, I-40129 Bologna, Italy*

[12]*Institute of Astronomy, University of Cambridge, Madingley Road, Cambridge CB3 0HA, UK*

[13]*Kavli Institute for Cosmology Cambridge, Madingley Road, Cambridge CB3 0HA, UK*

[14]*ORAU/NASA Goddard Space Flight Cetner, Greenbelt, MD 20771, USA*

[15]*Department of Physics, Stockholm University, AlbaNova, SE-106 91 Stockholm, Sweden*

[16]*The Oskar Klein Centre for Cosmoparticle Physics, AlbaNova, SE-106 91 Stockholm, Sweden*

[17]*Department of Astronomy, Stockholm University, SE-106 91 Stockholm, Sweden*

[18]*Helsinki Institute of Physics, Gustaf Hällströmin katu 2, University of Helsinki, FI-00014 Helsinki, Finland*

[19]*Aalto University Department of Radio Science and Engineering, P.O. BOX 13000, FI-00076 AALTO, Finland*

[20]*Instituto Nacional de Astrofísica Óptica y Electrónica (INAOE), Apartado Postal 51 y 216, 72000 Puebla, México*

[21]*Finnish Centre for Astronomy with ESO (FINCA), University of Turku,Väisäläntie 20, FI-21500 Piikkiö, Finland*

[22]*Dipartimento di Fisica e Scienze della Terra, Università degli Studi di Ferrara e Sezione INFN di Ferrara, via Saragat 1, I-44100 Ferrara, Italy*

[23]*Haverford College Astronomy Department, 370 Lancaster Avenue, Haverford, PA-19041 Pennsylvania, USA*

[24]*Physics Department, California Polytechnic State University, San Luis Obispo, CA 94307, USA*

This paper has been typeset from a TEX/LATEX file prepared by the author.